Accelerated permafrost thaw and increased drainage in the active layer

Responses from experimental surface alteration

Zastruzny, Sebastian F.; Ingeman-Nielsen, Thomas; Zhang, Wenxin; Elberling, Bo

Published in:
Cold Regions Science and Technology

Link to article, DOI:
10.1016/j.coldregions.2023.103899

Publication date:
2023

Document Version
Publisher's PDF, also known as Version of record

Cold Regions Science and Technology 212 (2023) 103899

Contents lists available at ScienceDirect

Cold Regions Science and Technology

journal homepage: www.elsevier.com/locate/coldregions

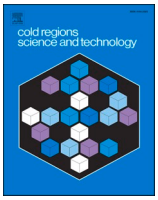

Accelerated permafrost thaw and increased drainage in the active layer: Responses from experimental surface alteration

Sebastian F. Zastruzny [a,*], Thomas Ingeman-Nielsen [b], Wenxin Zhang [c], Bo Elberling [a]

[a] Department. of Geosciences and Natural Resource Management, Center for Permafrost (CENPERM), University of Copenhagen, Øster Voldgade 10, DK-1350 Copenhagen, Denmark
[b] Department of Civil Engineering, Technical University of Denmark, 2800 Kgs. Lyngby, Denmark
[c] Department of Physical Geography and Ecosystem Science, Lund University, Sölvegatan 12, 223 62 Lund, Sweden

ARTICLE INFO

Keywords:
Permafrost degradation
Simulations
Water flow
Active layer dynamics

ABSTRACT

Erosion and infrastructure in the Arctic can change the thickness of the active layer which can subsequently alternate the thermal-hydrological regime and change the drainage patterns on slopes. Previous studies have shown that drainage can either decrease due to the movement of water occurring in deeper soil layers with lower permeability or increase due to the formation of features like gullies and channels.

In a field experiment conducted in Qaanaaq, Greenland, the surface topography was altered by adding 35 cm soil in one treatment, removing 33 cm in another, while an untreated plot measuring 10 × 10 m was maintained for comparison purposes. The temperature and water content of these plots were monitored in the three following years. Based on field measurements, a 1-dimensional model was set up in CoupModel to simulate the field experiment and quantify changes in the thickness of the saturated zone and drainage as a consequence of the treatment.

Both field observations and simulations show that the addition and removal of soil changed the thickness of the saturated layer in the active layer, which changed the thermal properties in the soil and, thus, the response of thawing or recovery of permafrost. The simulations showed that during the summer depressions there were higher water contents, which accelerated warming of the soil and increased permafrost thawing of 35.7 cm in depth. In contrast, raising the soil surface aggregated only 19.8 cm of permafrost due to higher buffering from lower water contents. Changed active layer thickness altered the thickness of the saturated zone, leading to changed drainage patterns: In depressions, first drainage occurs three days earlier, and maximum daily drainage is increased by 154% as compared to ambient conditions. In contrast, raising the surface delayed the runoff from the plot by up to eight days, and decreased the maximum daily drainage to 72%. Effects of the treatment were most pronounced during the first year after the experiment, with diminishing effects during the consecutive year as the system equilibrated to the new state. Results from our study can advance our understanding of impacts of both natural and human-induced surface alterations on active layer thickening and water movement in permafrost-affected areas, which ultimately affect the entire ecosystem and the living conditions for local communities.

1. Introduction

During the past decades, the Arctic has been undergoing many environmental changes, that include increasing temperatures (IPCC, 2021), increase in total precipitation (Box et al., 2019), and intensity of precipitation events (Bintanja and Selten, 2014). Permafrost, soil that remains below 0 °C for at least two consecutive years (Permafrost Subcommittee, 1988), is present in 26% of the northern terrestrial hemisphere (Obu et al., 2019) and is showing signs of warming across the arctic (Biskaborn et al., 2019). This leads to a deeper active layer (Strand et al., 2020), which in turn changes the soil characteristics and stability (Hjort et al., 2018). Closely connected to changes in the active layer are hydrological processes, which are controlled by precipitation and redistribution of snow (Young et al., 2013).

Permafrost landscapes are at risk of degradation due to changes in the climate (Karjalainen et al., 2020; Lantz et al., 2009). Lafrenière and

* Corresponding author at: IGN at Copenhagen University, Denmark.
E-mail address: sfz@ign.ku.dk (S.F. Zastruzny).

https://doi.org/10.1016/j.coldregions.2023.103899
Received 14 March 2023; Received in revised form 4 May 2023; Accepted 17 May 2023
Available online 19 May 2023

Lamoureux (2019) summarized the interplay between geomorphology and hydrology and distinguishes between 'thermal perturbation', a response from changed climate conditions at the surface, changing the extent of soil thaw during the melt season, and 'physical perturbation' to describe "processes that result in alteration of surface materials in such manner that soil and surficial material is laterally dislocated or removed". The latter can occur due to different forms of erosion or subsidence ('lowering' of surface topography) (Ingeman-Nielsen et al., 2018; Lal, 2019), such as retrogressive thaw slumps (Balser et al., 2014), active layer detachments slides (Lewkowicz, 2007), or the building of foundations ('raising' of surface topography) (Clarke, 2007). Those changes can have several effects, such as increased rates of erosion (Schädel, 2022), ecosystem responses (Vincent et al., 2012), river-system sediment load (Beel et al., 2018) and increased damage to infrastructure located in the permafrost zone (Hjort et al., 2022; Jorgenson et al., 2010), all resulting in challenges for local communities.

A particular effect are changes in the hydrological processes and flow paths (Kurylyk et al., 2014a; Lafrenière and Lamoureux, 2019; Sjöberg et al., 2021). The water in permafrost areas is classified according to its relative position as supra-, intra-, and sub-permafrost groundwater (Woo, 2012). The supra-permafrost aquifer is limited by the extent of the active layer, and as such, relatively thin, and changes in the order of centimeters can have large consequences for the total drainage from the active layer (O'Connor et al., 2019). The flow dynamics in the active layer are changing, allowing different flow depths and timings, leading to non-linear responses between rising temperatures and permafrost thaw (Connon et al., 2018; Frampton et al., 2012).

Groundwater flows in the active layer have previously been investigated in many field studies (Beel et al., 2018; Lamhonwah et al., 2017), with an increasing number of these studies using physical models to describe the drainage dynamics (Evans and Ge, 2017; Lamontagne-Hallé et al., 2018) and the overall permafrost hydrology (Walvoord and Kurylyk, 2016). Until recently, simulating heat and water fluxes, including freeze-thaw dynamics under unsaturated conditions, has posed challenges for such models (Kurylyk and Watanabe, 2013). But recently, models have been used to investigate the supra-permafrost dynamics (Atchley et al., 2015; Schuh et al., 2017), however this work often lacked validation of the model against field observations (Kurylyk et al., 2014b), and have only been able to present generalized tendencies.

Using validated model simulations, Liljedahl et al. (2016) showed that for areas where ice wedges are found, permafrost degradation is associated with changes in surface runoff and conclude that increased variability of the surface leads to non-homogeneous snow distribution, and in turn, is able to significantly increase the runoff. Similarly, measurements by Lafrenière and Lamoureux (2019) show that disturbances in the landscape can increase daily discharge by up to four times. The importance of the active layer thickness on the groundwater flow has further been demonstrated by O'Connor et al. (2019), who showed that besides the soil properties of the active layer, the thickness of the saturated zone exerts a major control on the groundwater flow.

With the arctic warming twice as fast as the global mean temperature (Smith et al., 2015), a range of critical questions mentioned above appear unanswered, not the least in relation to existing and future infrastructure. Lack of field data, longer time series and impact assessment of future implications of warming is of urgent need in many remote settlements of the Arctic. Uncertainness in relation to permafrost hydrology, water balance, and the links between local construction work and downslope implication have all been motivating factors for our planned work in Qaanaaq.

In this study we investigate the temperature trends over the last 70 years in Qaanaaq, a small settlement where soil stability and surface near water creates problems for infrastructure, and is considered a concern for people living in the town. Moderate perturbations ('raising' and 'lowering' of the surface) are one of the concerns, and here we present a field experiment, where such moderate physical perturbations are created under controlled conditions and the response in terms of subsurface/ground temperatures and the soil water contents have been monitored for three consecutive years (2018–2021). To quantify the resulting differences in drainage from the scenarios, the 1D-physical model COUP (Jansson, 2012) was calibrated and validated against field data, and subsequently used to simulate changes in the movement of the frost and water table, allowing to predict variations in drainage behavior between the scenarios. The work was made in order to address the following research questions:

1. Is the climate in Qaanaaq showing signs of warming and at what rate?
2. Which effects do physical perturbations have on seasonal variations of soil temperatures and water content?
3. How are these variations influencing the permafrost thawing and soil drainage?
4. What are the dominating parameters when simulating the impacts of physical perturbations on soil temperature and soil moisture with a 1-D process-based soil model?

2. Methods

2.1. Field site descriptions

The study site is located near Qaanaaq (77°28′00″N 69°13′50″W), a town with 619 inhabitants in 2021 (Avannaata Kommunia, 2023) located in NW Greenland at the Inglefield Gulf (Fig. 1). The climate is classified as polar tundra (Kottek et al., 2006). The climate normal (1991–2020) exists only for the Thule Airbase ('Pituffik') located ca. 100 km further south, and represents an annual average temperature of −10.2 °C and a reported average annual precipitation of 149.4 mm/year (Cappelen and Drost Jensen, 2021). A large portion of winter precipitation is redistributed and blown out to sea, decreasing the snow thickness during winter significantly. The cold temperatures lead to the soil being underlain by continuous permafrost (Obu et al., 2019). The underlying bedrock consists of Archean gneisses, covered by Meso- to late Proterozoic sedimentary rock (shale, sandstone and conglomerates) (Dawes, 2006; Henriksen et al., 2009). The surrounding tundra soil consists of marine deposits and raised delta terraces that have high contents of finer soil material. The community is partially built on the alluvial fan of a river where the soil is dominantly coarse grained sand and gravel, making it the only larger community in Greenland that is built on sediment instead of hard rock. This condition, together with the steep relief that spans from sea level to 87 m.a.s.l., leads to specific problems with the infrastructure. Many houses in the city have settlement problems (Hendriksen and Hoffmann, 2016), which are associated with the thaw of permafrost (Matzner and Borken, 2008).

Another challenge to the infrastructure comes from the swelling of the local rivers that occur in some years as a result of rapid glacier thaw (Kondo et al., 2021), resulting in quick erosion of the banks, putting houses, roads, and bridges placed in the vicinity at risk. Regular exfiltration from the active layer occurs throughout the town at irregular intervals being less destructive than flooding of the river, but nevertheless problematic for the inhabitants in the form of muddy or frozen patches. Further problems to the local infrastructure is associated with the damage caused by subsidence, and the formation of ponds on the hill sides of buildings that are not raised, leading to damages in the building material and mold in the houses. (Hendriksen and Hoffmann, 2016) (Fig. S1).

2.2. Field & laboratory measurements

The surface of the slope in the east part of the town was visually described in 5 m intervals along a transect from the coast to 800 m inland with a 1 m^2 frame, where soil cover, vegetation, and water tracks were registered. Across the slope, 29 volumetric soil samples were collected in September 2017 (Fig. S2) with a hammer and soil corer with

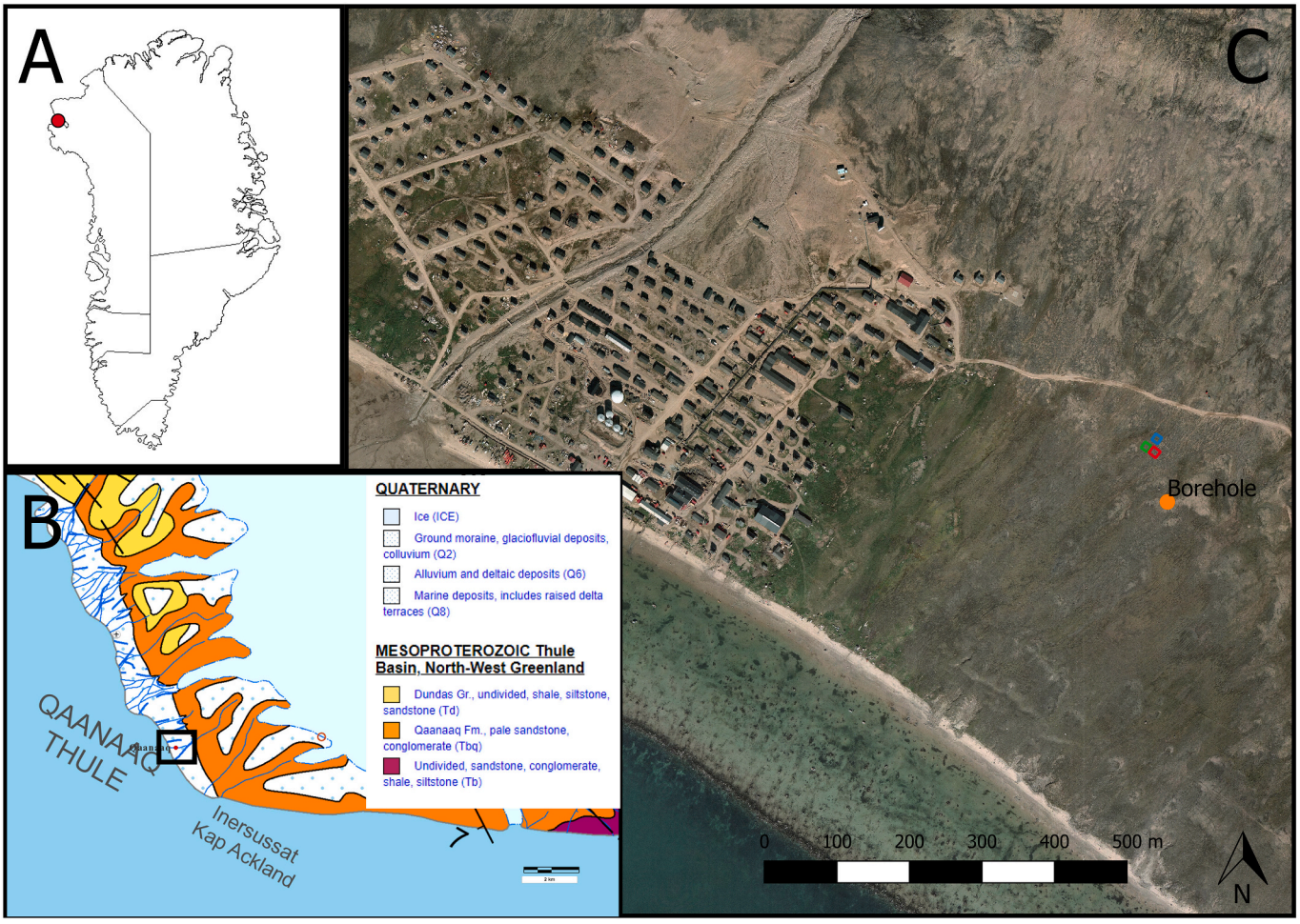

Fig. 1. Location of the field site: A) Location of Qaanaaq in Greenland; B) Close up of the geological setup around the city (GEUS, 2012); C) Location of treatment plots (colored squares) and borehole located east of the city (Ortho photo from Asiaq, Greenland Survey).

an inner diameter of 60 mm. To describe the heterogeneity of soil properties in the active layer, samples were dominantly collected at the depth between 0.2 and 0.3 m with irregular intervals along a transect normal to the slope, and seven samples were collected from a depth between 0.5 and 0.75 m at individual locations. To gain information for deeper layers, undisturbed, frozen core samples from one borehole of a drilling campaign in 2017 (Ingeman-Nielsen et al., 2020) were added to the laboratory analysis from the available core samples at the depth of 1.43, 1.75, 2.53, 2.76, 3.28 m. All the samples were kept frozen from the moment of extraction until analysis in the laboratory. Porosity was calculated assuming the typical grain density for quartz of 2.65 kgm^{-3} (Blume et al., 2011) and water content was measured gravimetrically following standard procedures (Blume et al., 2011). Samples were subsequently freeze-dried and analyzed for soil texture, first with sieving components for >2 mm and consecutive analysis by laser refraction analysis (Malvern Mastersizer 2000). Subsamples of each probe were analyzed for total carbon and nitrogen content by Dumas Combustion on an elementary analyzer (1110CE, Thermo Electron, Milan).

During the same field campaign in August 2017, 29 sensors (Decagon TE5) were installed in sensor columns consisting of six positions across the slope from nearshore to 600 m inland. For each column, five (QAA5 with four) sensors were installed in depth intervals of 0.10 cm or 0.20 cm, exceeding the thickness of the active layer during installation, reaching a minimum of 80 cm and a maximum of 100 cm. Those sensors monitored the soil temperature and (unfrozen) water content in the active layer during one year (Sept. 2017- Sept. 2018), before being removed.

In September 2018, an experiment was established, 100 m east of the town on a south facing slope with a gradient of 5% and 420 m away from the coast. The location was chosen based on fairly homogeneous soil properties being representative for the slope and accessibility by equipment. Using an excavator, the top 10 cm of soil were removed on two plots each measuring 10 × 10 m. A soil pit with a depth of 30 cm was excavated on one plot and the homogenized soil was transferred to the second plot. The removed topsoil was redeposited on both plots. No vegetation cover was established on the plots, but carbon content in the top soil is assumed to represent ambient conditions. A third plot of the same size was marked and left unaltered as a control plot (Fig. 2). Locations and dimensions of the plots were measured by GNSS (Garmin GPSMAP 63S) and optical level, conducted one week after the installation to allow for initial settlement of the soil. The surface change on the plots were 0.33 (±0.19) m and 0.35 (±0.12) m, for the low (L) and high (H) plot respectively. At the center of each plot, pits were dug to collect volumetric soil samples (diameter 80 mm) at 0.3, 0.6, 0.9 m to test hydraulic conductivity (Meter, KSat) and retention parameters (Meter, Hydrprop2) in the laboratory. The experiment plots were equipped with the same type of sensor that was installed on the slope (Decagon TE5), monitoring the soil temperature and (unfrozen) water content at six depths between 0.2 m to 1.6 m, at hourly intervals in the center of the plot and in a distance of 1 m downslope of the plot. Five frost tubes were installed on each plot, allowing for manual monitoring of the frost table across the plots. (Fig. S3).

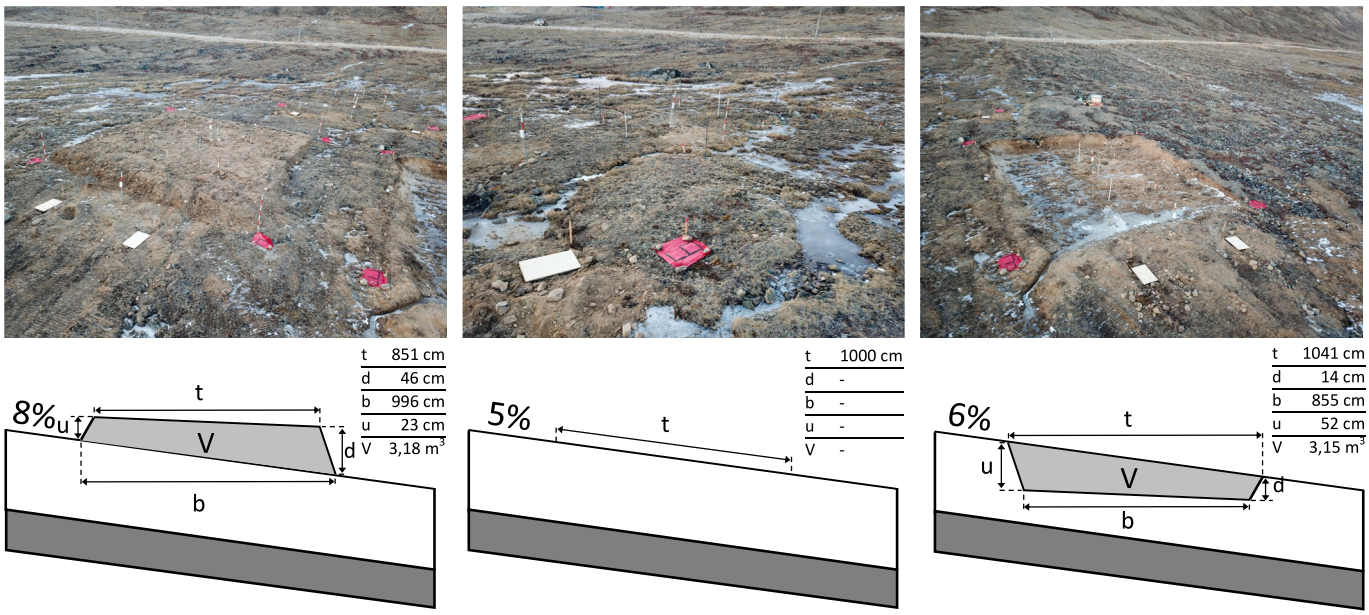

Fig. 2. Experiment Setup in Qaanaaq with treatment plots for elevated ('High') plot, unaltered ('Control') plot, and lowered ('Low') plot. *Top*: Picture of the field plots; *Bottom*: Profile, normal to the slope, with measurements.

2.3. Climate data

In order to investigate long-term trends in the air temperature since 1950, various datasets from field stations in the proximity were used (Cappelen and Drost Jensen, 2021; Menne et al., 2012). Time spans of datasets varied (Fig. S4), but made it possible to compile a continuous dataset of measurements for daily air temperature over the period 1950 to 2020. All stations that were available during any given day were aggregated to an unweighted mean of that day, resulting in a full time series of averages. To control that the average is representative for each single station, the correlation was evaluated by the coefficient of determination (R^2) (von Storch and Zwiers, 1999). From the daily average, the annual freezing and thawing degree days were calculated (Vaughn, 2005). Additionally, the maximum and minimum temperatures of each year were calculated based on monthly averages.

Results from other locations in Greenland suggest a change in trends occurring around the year 1990 (Hansen et al., 2006; Westergaard-Nielsen et al., 2018). Taking this into account, the time series were split into pre-1990 and post-1990 datasets and from thereon analyzed individually. First-order regression functions were fitted to monthly mean values, and tested for significant changes over time including both annual, as well as seasonal (summer, winter) changes ($p < 0.05$).

Meteorological driving data for the model (air temperature, relative humidity, precipitation and wind speed) was obtained from four different sources (Table 1, Fig. S5). Next to the field site (distance 32 m) a weather station was installed measuring air temperature, relative humidity, wind speed, and direction, at 2 m elevation, as well as liquid precipitation with a tipping bucket pluviometer 1 m above ground. The snow depth was measured with a sonic range sensor (SR50) and surface temperature with a thermistor. Data from that field site was used for the simulation of scenarios (2018–2021). Measurements from a weather station at the airport located 4.5 km W from the field site were used for calibration and validation (2017–2018). For the spin up period (2000–2017) the air temperature from the Thule Airbase, located ca. 100 km south of the experiment location, was used. Minor data gaps were filled with data from the NCEP-NCAR reanalysis (Kalnay et al., 1996). All climate drivers were comparable and no correction between the sources was necessary (Fig. S6).

2.4. Modeling

2.4.1. Setup

In order to investigate the interactions between thawing depth, water level, and total runoff, a model was set up to include the water and heat flow processes at the field site in more detail. To simulate these processes, the CoupModel (Jansson, 2004), a one dimensional processed-based, numerical ecosystem model was used. The CoupModel includes a fully coupled water and heat transfer module, that has been successfully used in several studies investigating the subsurface processes in the arctic (Hollesen et al., 2011; Rasmussen et al., 2018; Zhang et al., 2019).

The specific model setup is a 1-dimensional column, consisting of 31 layers with increasing thickness from 0.1 m to 2 m from surface to bottom, extending to a depth of 20 m. The model spun up in only two years running time (01.08.2015–01.08.2017). The short spin up was achieved by starting the model with an initial temperature profile that was close to measurements taken in the borehole in August 2017, thus omitting long runtimes to achieve the thermal state encountered at the beginning of the calibration period. Tests with longer spin up periods running from 2000 from uniform thermal conditions (av. annual

Table. 1
Sources and time spans for meteorological driving data. 'Field Site' is a locally installed weather station for this work, 'Qaanaaq Airport', is station Number 4205 (Cappelen and Drost Jensen, 2021) and Thule Airbase is THULE OP SITE (Menne et al., 2012).

Parameter \ Weather station	Field Site	Qaanaaq Airport	Thule Airbase
Temperature	03.08.2018–28.07.2021	01.01.2017–14.07.2019	04.07.2000–20.06.2018
Relative humidity	03.08.2018–01.03.2020	01.01.2017–30.12.2019	n.A.
Precipitation	03.08.2018–01.03.2020	01.01.2017–30.12.2019	14.07.2000–20.06.2018
Wind speed	03.08.2018–01.03.2020	01.01.2017–30.12.2019	n.A.

temperature of −11.2 °C) were tested, but showed no improvement of the calibration results (Fig. S7). Initial liquid water contents were in accordance with water content measured in the borehole for depth below 1.5 m, apart from two peaks occurring at 2 m and 3.25 m depth, and with the water content measured in the active layer (Fig. 3a).

Grain size distribution (Fig. 3b) is measured at eleven depths and linearly interpolated in-between measurements. For the deeper layers (> 1 m) the grain size distribution is used to estimate the porosity and water retention parameters (Brooks and Corey, 1966) and saturated hydraulic conductivity (Fig. 3c) using pedo-functions (Rawls et al., 1982). For the surface near layers (<1 m) water retention curves and hydraulic conductivity were measured. The content of organic matter and quartz (Fig. 3d) is used to estimate the matrix thermal conductivity (Fig. 3e), using the approach from (Balland and Arp, 2005). Organic content is calculated from the measured content of carbon by multiplying with the factor 2 (Pribyl, 2010) and the quartz content is estimated assuming that the sand fraction of the soil contains 70% quartz (Garzanti, 2019).

The following paragraph sums up key components used in the presented model. A more detailed description can be found in (Jansson, 2004). The model calculates soil water flux q_w (ms^{-1}) between soil layers assuming that the laminar matrix flow and is calculated by using the equation by Richards (1931):

$$q_w = -K_{H,\vartheta}\left(\frac{\Delta p}{\Delta z} - 1\right) - D_v\frac{\partial c_v}{\partial z} \quad (1)$$

With $K_{H,\vartheta}$ (ms^{-1}) being the unsaturated hydraulic conductivity, p the pressure head (cm), z the depth (m), D_v the diffusion coefficient for vapor (m^2s^{-1}) and c_v the concentration of vapor in the soil air (m^3m^{-3}). Under frozen conditions $K_{H,\vartheta}$ is reduced after a specified freezing function, based on the amount of ice. The model includes freeze-thaw dynamics that are treated analogous to drying-wetting, changing the hydraulic properties and takes into account both sensible and latent heat.

Soil heat flux q_h (Wm^{-2}) obey Fourier's Law and include thermal conductivity, based on temperature gradients (dT/dz) and convective flows after

$$q_h = -K_T\frac{\Delta T}{\Delta z} + C_w T q_w + L_V q_v \quad (2)$$

With K_T being the effective thermal conductivity of the bulk soil ($Wm^{-1}\,°C^{-1}$), C_w the heat capacity of water ($Jm^{-3}\,°C^{-1}$), L_V the latent heat of vapor (Jm^{-3}), and q_v the vapor flux (ms^{-1}),. K_T is calculated as the weighted geometric average of the constituents' conductivities.

The lower boundary is set to a constant temperature of −8.45 °C which was observed in local boreholes to show zero annual amplitude (Ingeman-Nielsen et al., 2020). The model surface uses an integrated coupled surface/subsurface model, which allows for meteorological forcing, and includes a surface energy- and mass balance including evaporation, snow cover and surface ponding and reduced thermal conductivity due to ground ice and an organic layer.

Evaporation from the soil surface is calculated using the Penman-Monteith eq. (1965) using the net radiation based on the latitude and sunshine hours (Goudriaan and Van Laar, 2012), soil heat flux, vapor pressure calculated surface resistances, and several physical constants.

During winter, snow acts as a storage for water and as a thermal insulator, reducing the coupling between air temperature T_{Air} and surface temperature. Precipitation is partially deposited as snow when T_{Air} is below 2 °C and fully deposited below 0 °C. The amount of snow melting M (kg) is controlled by T_{Air}, global radiation R_{is} ($Jm^{-2}\,day^{-1}$) and heat flux from the soil $q_h(0)$ (Wm^{-2}):

$$M = M_T T_{air} + M_R R_{is} + \frac{f_{qh} q_h(0)}{L_f} \quad (3)$$

With M_T ($kg°C^{-1}\,m^{-2}\,day^{-1}$) a function based on an empirical parameter m_T and M_R (kgJ^{-1}) a functions including empirical parameters and the age of snow, f_{qh} (−) a scaling coefficient and L_f the latent heat of freezing (Jkg^{-1}).

Measured winter precipitation is reduced by a factor f when T_{Air} is below 0° to account for snowfall and redistribution due to strong winds. The factor f is found by an iterative stepwise process that compares the simulated to the observed snow depth at the end of winter. A value of 0.2 was found to be best fitting.

$$Prec = \begin{cases} T_{Air} > 0°C\ Prec = Prec_{measured} \\ T_{Air} \le 0°C\ Prec = Prec_{measured} \cdot f \end{cases} \quad (4)$$

When the net precipitation/melting water flux into the ground exceeds infiltration capacity within the soil, a surface pool is created, that may infiltrate with delay or drain as surface runoff q_{Surf} (ms^{-1})

$$q_{Surf} = a_{surf}\left(W_{pool} - w_{max}\right) \quad (5)$$

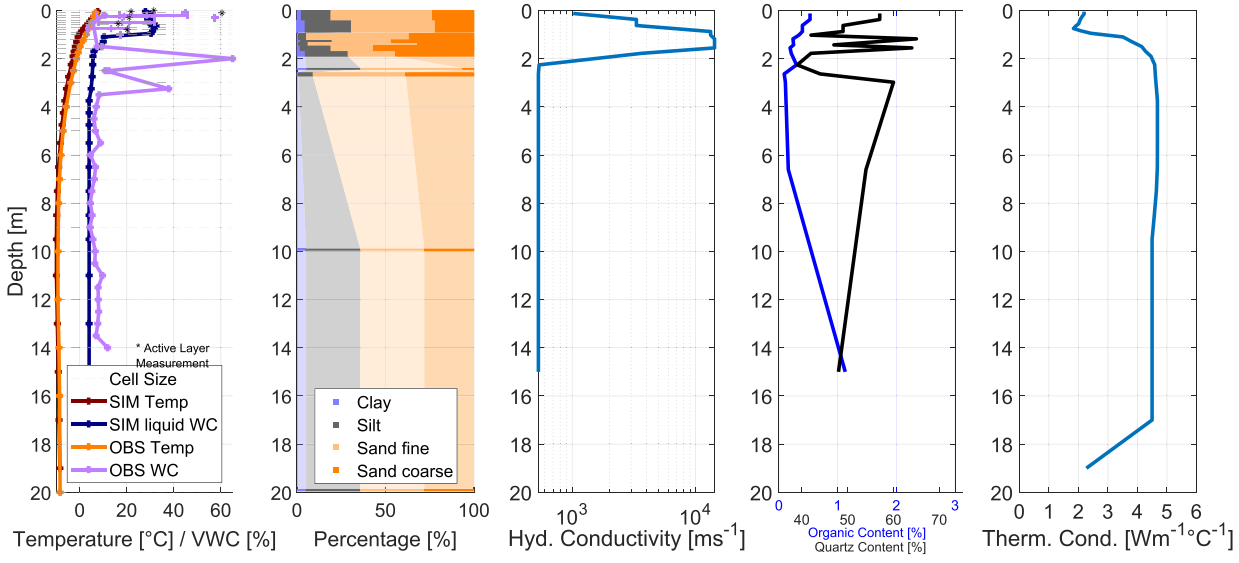

Fig. 3. Depth specific model parameters: Initial conditions (a) after spin up (SIM) compared to measured conditions in the field (OBS). Grain size distribution (b) is used to estimate hydraulic conductivity (c) below 1 m, above it is based on measurements of hyd. conductivity. Estimated quartz content and measured carbon content (d) is used to determine bulk thermal conductivity (e) at initial conditions.

Table 2
Parameters used for calibration and selected parameter ranges.

Parameter		Value			Function	Ref.
Name	Symbol/ Unit	Min	Start	Max		
HighFlowDampC	$c_{\theta,I}$ [%]	5	30	40	Dampening factor corresponding to the blockage of ice in the high flow domain.	1
C frozen max dampening	C_{md} [−]	0.2	0.9	0.9	Frozen Surface Dampening Function - Reduce thermal cond. at the surface	2
C frozen surface correlation	C_f [°C^{-1}]	0.2	0.2	0.8	Frozen Surface Dampening Function - Reduce thermal cond. at the surface	2,3
Melt CoefGlobRad	m_T [kgJ^{-1}]	0.5 × 10^{-7}	1.5 × 10^{-7}	4.5 × 10^{-7}	Control snow melt velocity as function of global radiation	1
Crit Snow Depth	z_{cov} [m]	0.01	0.01	0.4	Thickness of full snow, accounts for barrier between T_{air} and T_{soil}.	Field Observations
Organic layer thickness	z_{hum} [m]	0.06	0.1	0.1	Thickness of humus layer for therm prop., accounts for barrier between $T_{surface}$ and T_{soil}.	Field Observations
Freezepoint F0	d_3 [−]	2	10	10	Freezing function – connecting liquid water content to change of energy storage	2
Freezing start temp	t_f [°C]	-1	0	0	Freezing function – freezing point depression	Field Observations
Albedo Dry Soil	a_{dry} [%]	10	35	35	Albedo of Dry Soil	4
CloudFmean	n_c [−]	0.2	0.2	0.9	Mean cloudiness as fraction	Analysis of 5
Max Surface Excess	s_{excess} [mm]	1	2	3	Maximum water deficit at the surface, used in the PM equation formula for the ET	2

References for parameter ranges: 1) (Jansson, 2012); 2) (Wu et al., 2011); 3) (Zhang et al., 2018); 4) (Dobos, 2020); 5) (Kalnay et al., 1996)

, where a_{Surf} (s^{-1}) is an empirical coefficient, W_{pool} is the total amount of water (mm) and w_{max} is the specified maximum amount of water the surface can hold (mm). The latter is dependent on micro topography at the field site and is used in the calibration.

Lateral drainage q_{lat} (ms^{-1}) is calculated based on a linear model that allows for drainage between the saturation depth z_{sat} (m) and the drainage level z_p (m), taking into account the saturated hydraulic conductivity $K_{H,s}$ (ms^{-1}) and thickness of each soil layer z (m) of the column. The slope at the field site is translated to the model domain by placing the drainage level z_p (m) 20 m below the model surface and using a drainage distance d_p of 400 m, corresponding to a slope of 0.5. (z_p/d_p).

$$q_{lat} = \int_{z_p}^{z_{sat}} K_{H,s} \frac{(z_{sat} - z_p)}{d_p} dz \tag{6}$$

At the field site only isolated small vegetation is found and on the treated experiment plots vegetation and roots were heavily disturbed, thus vegetation and roots were not included in the model.

2.4.2. Model calibration and evaluation

The model is evaluated based on the performance of simulated values (SIM) against observed values (OBS) of soil temperature (TEMP) and liquid volumetric water content (VWC). Goodness of fit between OBS and SIM is evaluated by the Nash Sutcliff Efficiency (NSE), a dimensionless indicator, which is the ratio between the Root Mean Square Error (RMSE) and the Standard deviation (SD) of the data (Nash and Sutcliffe, 1970) defined as:

$$NSE = 1 - \frac{\sum_{i=1}^{N} (OBS_i - SIM_i)^2}{\sum_{i=1}^{N} (OBS_i - \overline{SIM})^2} = 1 - \left(\frac{RMSE}{SD}\right)^2 \tag{7}$$

For the calibration period running from Sept 2017-Sept 2018, simulation results were compared against the average from six different locations separated into four different depth (0.2, 0.4, 0.6, 0.8 m). The model was optimized based on the means, but the variation between the individual stations was kept to evaluate the amplitude occurring due to the natural variation found at the field site.

Based on the conceptual model, parameters that can influence the hydrothermal soil regime were selected, and a manual sensitivity analysis was performed prior to the calibration to identify and rank the most important parameters, by comparing the NSE of individual runs. The 11 most sensitive parameters (Table 2) were then used with the ranges set large enough to allow for physical possible values. Using a general likelihood uncertainty estimation calibration method as described by Wu et al. (2011), the model went through 20.000 simulations sampling uniform-randomly through the parameter ranges specified to identify the best performing set of parameters.

After the multi run, the ten best performing runs were selected based on the NSE > 0.96 and R^2 > 0.97 of the temperature at 0.2 m and 0.8 m, respectively. All ten runs were subsequently used for scenario runs to account uncertainty of the model runs.

2.4.3. Model scenarios

To simulate the altered active layer thickness the model was split up in three scenarios at 01.09.2018 (Fig. 4). For the scenario 'high scenario', three new soil layers (thickness each 0.1 m) were added on the

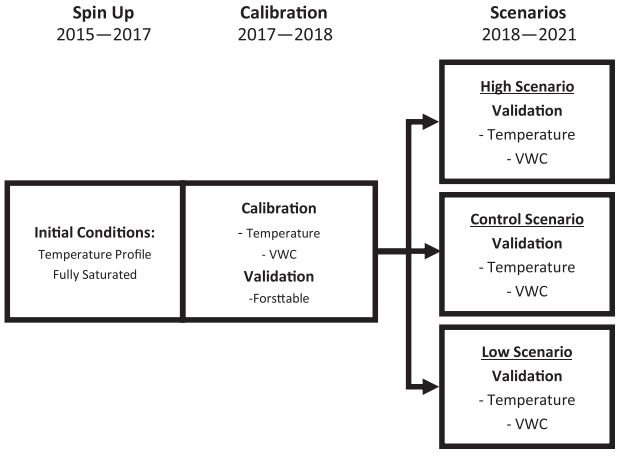

Fig. 4. Model setup scheme. The ten best performing runs from 01.08.2015 to 31.08.2018 were used to present average numbers used in the study. On 31.08.2018, the model was stopped and final readings were extracted. Layers are added/removed at the top of the model to create the two scenarios. The model is restarted on 01.09.2018 with the cell specific mean of the final reading as initial conditions and is run with the parameter sets of the ten best performing runs.

top with the soil conditions being equal to the previously topmost layer. Similarly, to simulate decreased active layer thickness due to erosion, three layers were removed from the original model, so that a previously covered soil layer became the surface layer making up the 'low scenario'. A further scenario without any changes was also kept as the 'control scenario'. The initial conditions (temperature and water content) of the scenario runs were set identical to the final conditions for the run up until 31.08.2018.

3. Results

3.1. From observations

3.1.1. Climate trends in Qaanaaq

Each of the six different climate stations correlated well to the calculated mean ($R^2 > 0.99$), with the exception of the climate station located in Thule Airbase, which diverted during the year 2011 thus reducing the coefficient of determination to 0.98. (Fig. S4). Despite the diversion in 2011, the climate means are used below to evaluate the climate trend in Qaanaaq.

For the first period, from 1950 until 1990, the mean annual temperature increased from −11.5 °C to −10.2 °C (+1.3 °C), corresponding to an annual change of +0.033 °C per year. The warmest month in every year was either July or August and the coldest month was December, January or February. Over 40 years, the summer months (July and August) showed an increase in air temperature from 11.1 °C to 15.2 °C (+4.1 °C), while the winter (December, January, February) cooled from −35.2 °C to −38.3 °C (−3.1 °C).

The second period, stretching from 1990 until 2020, kept the overall annual trend (+0.047 °C/a), increasing from −10.2 °C to −8.8 °C (+1.4 °C). Warmest and coldest month remained the same as before, but the trend reversed: The average temperature during the warmest month decreased from 15.2 °C to 11.5 °C (−3.7 °C), but for the coldest month the temperatures got warmer, increasing from −38.3 °C to −31.2 °C (+7.1 °C). (Fig. 5, top).

The ratio of thawing to freezing degree days (Fig. 5, bottom) confirms the warming trend since 1990. Between 1950 and 1990 the ratio was at average at −0.08 with values <−0.11 only in 1957 and 1988. For the period after 1990, the average was −0.11, indicating longer and warmer thawing phases with especially the years between 2005 and 2012 having low ratios below −0.13, exceeding values that have only occurred three times before (1957, 1988, 2003).

3.1.2. Surface and soil textures

The surface was in places covered by tundra vegetation with a height of 10–15 cm and dominated by the following plant species: *Salix arctica, Vaccinum uliginosum, Polygonum viviparum*, while in other places, only rocks and pebbles cover the ground. In the lower part of the slope (200 m until from the coast), the surface cover was dominated by grass and individual hummocks. The soil shows signs of erosion in the form of larger cracks in the soil and active layer detachment faults occurring along a line normal to the slope 40 m from the coast (Fig. S1). Up the slope, the vegetation becomes sparser, and moss and pebbles dominate the ground. The hillslope is characterized by widespread occurrences of water tracks and rock lines of up to 1 m depth that occur on average every 20 m and were running parallel to the slope. These water tracks were filled with pebbles (up to 30 cm in diameter) and sometimes sealed with a fine sediment at the bottom.

Grain size distribution (Fig. 6) showed that the soil along the slope was largely dominated by fine-medium sand, and classified as silty sand with a total sand content >50%. Clay content in the top 3 m remained <8% for all samples. The average porosity was 35%, but exceeding 64% at individual locations, in coarse sand. The slope could be split into a fine-grain lower slope near the sea dominated by silt and clay, and a coarse-grain upslope area, more dominated by sand (Fig. S8). In the coarse dominated area soil pipes are found in the active layer, consisting of small pebbles and coarse sand, that allow for rapid water transport in lateral direction.

3.1.3. Regional soil thermal-hydrological regime

Soil temperatures in the active layer for the year 2017–2018 (Fig. S9) showed temperatures in the surface near soil (20 cm) ranging from −26.8 °C in the winter to +10.6 °C during the summer months. Intraday variations between the different locations lay within 3.7 °C during the

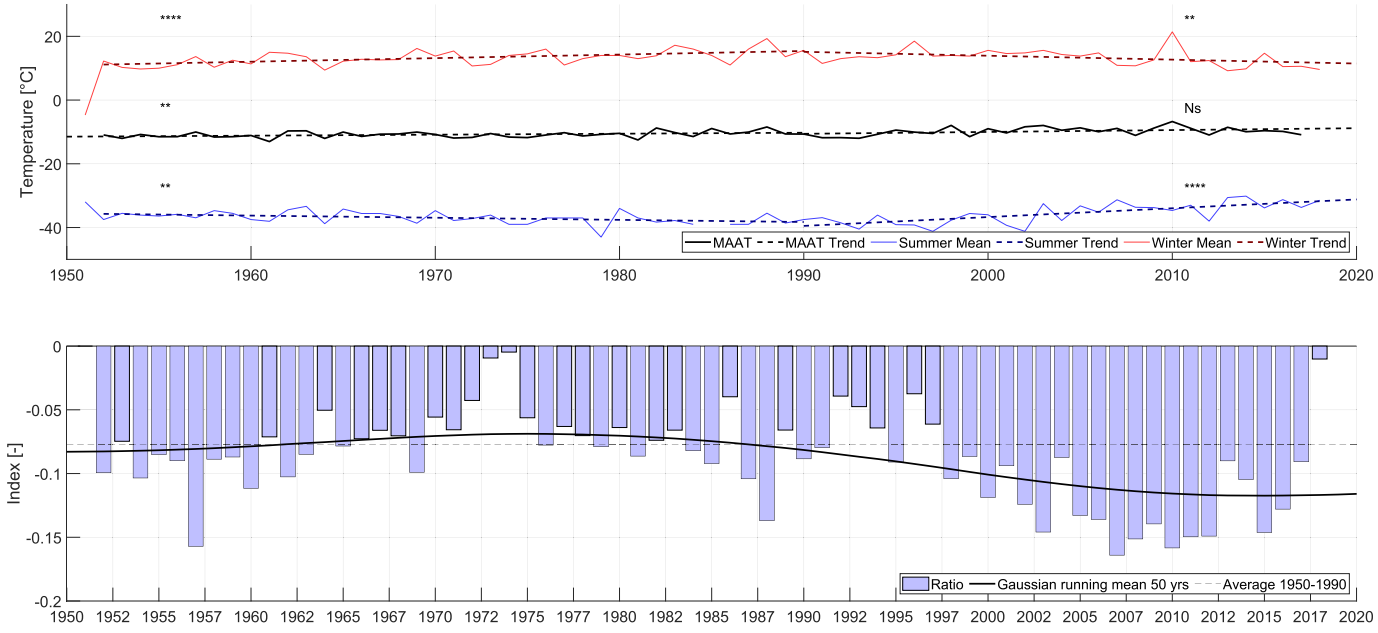

Fig. 5. Compiled temperature indexes for 70 years in Qaanaaq, based on six climate stations in the area. *Top:* Annual average air temperature (black), av. temperature of the warmest month (red) and the coldest month (blue). Trend lines are linear polynomial functions (p-tested for significance: Ns, $p > 0.05$; * $p \leq 0.05$; ** $p \leq 0.01$; *** $p \leq 0.001$; **** $p \leq 0.0001$) split in 1990. *Bottom:* Annual ratio of thawing degree days to freezing degree days and Gaussian running mean for the period of 50 years. Y line at 0.08 as the average value for 1950–1990.

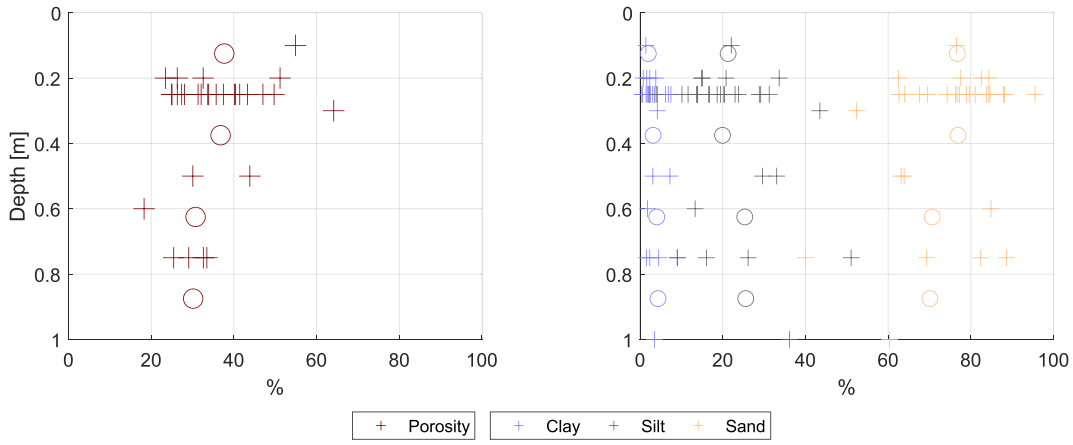

Fig. 6. Porosity and grain size distribution measured on 29 samples from the active layer collected across the field side (+). For the specification in the model unweighted depth averages for the depth intervals 0.0–0.24; 0.25–0.49; 0.50–0.74; 0.75–1.00 where calculated (o). Sample locations are shown in Fig. S2 and geographical distribution of the GSD in Fig. S8.

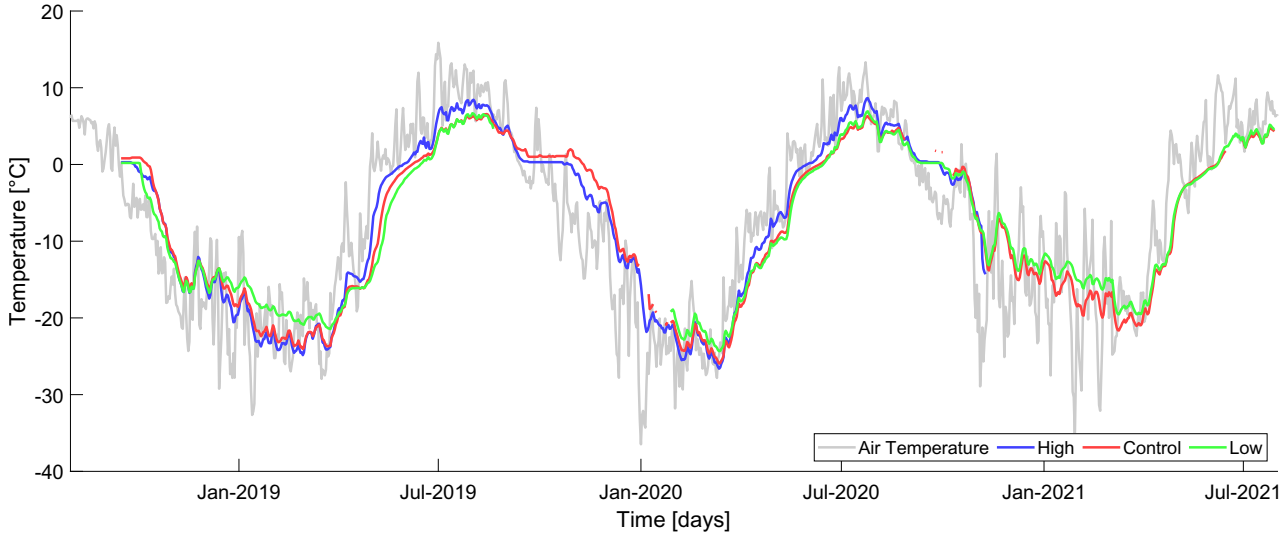

Fig. 7. Time series of soil temperature at 60 cm measured with installed soil sensors at the center of the high, control and low plot. Gray line shows daily air temperature at 2 m measured in a distance of 35 m to the experiment plots.

winter months and 4.4 °C during the summer months. Measurements of the soil water content indicate that maximum saturated water content exceeded 40% at some locations, but mostly remained between 26% and 35% during the thawed periods. A dedicated peak at the beginning of summer in response to snowmelt occurs on some surface near sensors, but dissipates within 4–5 days.

Time-lapse pictures and reports from the local population indicate that snow thickness rarely exceeds 0.5 m and most of the year barely covers the ground. The observed strong sea winds (velocity > 10 m/s, direction SE) in the area exceed threshold wind speeds of 9.9 m/s that are reported to redistribute even wet snow (Li and Pomeroy, 1997). The small topographic changes lead to a heterogeneous snow cover, with only depressions being snow covered throughout the winter. After the snowmelt and during intense rainfalls (i.e. saturation capacity of soil is exceeded) the soil becomes saturated and overland flow is occurring. This overland flow weakens the top soil and has been observed to contribute to erosion (Fig. S1). Parts of the slope are further drained by rock lines, moving water rapidly downslope in the form of surface flow.

3.1.4. *Active layer thickness*

Interpolation from soil temperature measurements on the slope (Fig. S10) allowed for the delineation of the active layer thickness for the period 15.08.2017 until 16.08.2018, which could be verified against steel rod measurements conducted on the measurements of solid ice in piezometers (Fig. S11). In 2017, freezing of the active layer began bottom up at the end of August, but the majority of freezing occurred top down to a depth of 1.00 to 1.50 m from 06.09.17 until 10.10.17. Thawing of the active layer began on 29.05.2018 for all locations and exceeded maximum thawing depth between 1.66 m and 2.15 m (mean = 1.88 m) at different locations on the slope at the end of August. Analysis of temperature loggers from nearby boreholes conclude similar maximum active layer thickness between 1.74 and 2.21 m (Ingeman-Nielsen et al., 2020).

3.1.5. *Results of the field experiment*

The change of the surface into a high plot (H) and low plot (L) had an effect on the thermal-hydrological regime of the soil when compared to the control plot (C) right from year one. Differences are illustrated by

Table 3
Monitored temperatures in 60 cm depth at the center and downslope of the treatment plots for the year 2019.

Measurement	High		Control		Low	
	Center	Downslope	Center	Downslope	Center	Downslope
Thawing [Date]	30.05.19	05.06.19	08.06.19	06.06.19	15.06.19	08.06.19
Freezing [Date]	29.10.19	n.a.	10.11.19	04.11.19	n.a.	01.11.19
Summer Average Temperature [°C]	4.81	n.a.	3.10	3.67	2.77	3.80
Winter Average Temperature [°C]	−22.20	−19.83	−21.64	−21.27	−19.10	−21.63

comparing the temperature and soil moisture at 60 cm depth in the three plots (Fig. 7, Table 3). At 60 cm depth H thawed 9 days earlier, and L thawed 7 days later than C, which is in line with the longer period of the snow. During the summer, H was 1.7 °C warmer than C, and the daily amplitude was 20% larger. L and C plot behaved very similarly during the summer.

Winter temperatures at L remained on average 2.8 °C warmer and the intra daily amplitude was 30% smaller than in the other plots. Winter temperatures at C and H had similar intra daily variation, with H being on average 0.6 °C cooler. Interpolations of the soil thermal regime (Table 4) indicated that in response to the surface change of 0.35 m, the H plot aggregated 0.33 m of permafrost in the first year and remained stable for the second year. On the L plot, the surface change of 0.33 m thawed 0.20 m permafrost in the first year and 0.28 m in the second year (Fig. S12). Water content during the summer did not differ significantly between the different plots and variations lay within 4%. During winter, unfrozen water content on the H plot was 5% lower than the other plots indicating that the water from the deposited soil had drained before freezing up in September.

3.1.6. Calibration / Validation results

The model performance (Fig. 8) for the soil temperature was acceptable with NSE reaching values >0.93 for both the calibration and the validation period. The simulation of soil moisture proved to be more challenging, but a match with the NSE > 0.88 for the calibration period, and NSE > 0.71 for the validation period could be achieved, with the exception of the water content at 1.2 m during the validation period, which only exceeded 0.63 (Table 5). The one poor performing point at 1.2 m achieved a value of NSE = 0.63. At this one point, the thawing of the soil is simulated to happen later than observed, which produced an offset during a period of one week, thus deteriorating the NSE value. The poorer match of water content compared to temperature is often observed in model studies (e.g. Okkonen et al. (2017)) and is related to the multitude of process involved in the water movement, and the rapid changes in the near surface layers, which are influenced by melting, evaporation, surface pooling. Furthermore, the performance of water content simulation is closely tied to the correct description of the soil water retention curve (Dye et al., 2009). We relate deviation in the model performance to omission of complex snow dynamics and heterogeneity. The water retention was primarily assessed by grain size distribution or measurement of point samples collected in the field. The described high heterogeneity of silt content in the active layer created a challenge for setting up a field representative model. To account for site-specific heterogeneity and model uncertainty a common practice is to select a set of best performing model runs to investigate effects (Jansson, 2012; Wu et al., 2011), in the current study 10 runs are selected and used for the consecutive scenario analysis.

Table 4
Interpolated maximum active layer depths in the center of the experiment plots and change to thawing depth of the control plot.

Year	Measurement [cm]	High	Control	Low
2019	Max Thawing Depth	180	213	233
	Difference to control plot	33	–	−20
2020	Max Thawing Depth	164	197	225
	Difference to control plot	33	–	−28

3.2. Model scenario results

The model is used to simulate the depth to the frost table (i.e. thickness of the active layer) and the depth to a free water table (i.e. saturated zone) and the resulting total runoff, separated into drainage through soil and surface runoff for the three scenarios high (H), control (C) and low (L).

3.2.1. Active layer thickness and water table

The maximum active layer thickness responded to the change in surface by aggregating new permafrost in the H scenario and thawing permafrost in the L scenario (Fig. 9). The quantification of this change in permafrost showed that in one year after the treatment the frost table moved up 19.8 cm in the H plot in response to a 30 cm change in surface, corresponding to 66%. For year two, the maximum active layer thickness was 18.0 cm, indicating that the equilibration to the new surface elevation happened roughly within one year (assuming similar climate the two years). On the L plot, the lowering of the surface by 30 cm yielded a thaw of permafrost exceeding 35.68 cm, thus 119% of the surface change in year one and a change of 39.18 cm (130%) in year two, even increasing thaw response in the permafrost.

A free water table (i.e. above the frost table) appeared at different dates and depths between the scenarios, and followed the frost table with thickness of ca. 10 cm until the beginning of August, when maximum active layer thickness was reached and the water table did not follow the frost table any longer. The water table was less affected by the changed surface elevation and the initial conditions were quickly changed by the first inflow of water from snowmelt occurring as soon as a free aquifer formed in late June.

The different response of the frost table and the water table resulted in variations of the duration and maximum thickness of the perched supra permafrost aquifer between the different scenarios (Table 6). In year one after the treatment (2019), the opening of the aquifer occurred first in L three days later in C and further eight days later in H, despite that water table was 47 cm closer to the surface in H than in L during the time of opening. In the following year (2020) the supra permafrost aquifer opened within three days of each other, with only C being three days earlier. The depth at which the water table formed moved downwards due to lower precipitation in later summer of 2019, but differences between the scenarios remained comparable to 2019.

The maximum thickness of the aquifer occurred usually towards the end of august, with the only exception in C in 2020, when maximum thickness occurred on 04.08.2020. The general trend showed that in H the aquifer was 5 and 8 cm thinner compared to C in 2019 and 2020 respectively and L was 5 and 3 cm thicker for the two years.

3.2.2. Runoff Patterns

The accumulated annual surface runoff was dominated by large flows at the beginning of summer (15.06.19 until 25.06.19) where 12.4, 14.2 and 15.1 mm runoff accumulated in the H,C and L scenario respectively. On all plots, 0.3 mm of surface runoff was equally noted after the complete freezing of the active layer at the end of October, when a short period with temperatures above 0 °C (24.10.19–26.10.19) allowed the melting of snow, and thus surface runoff.

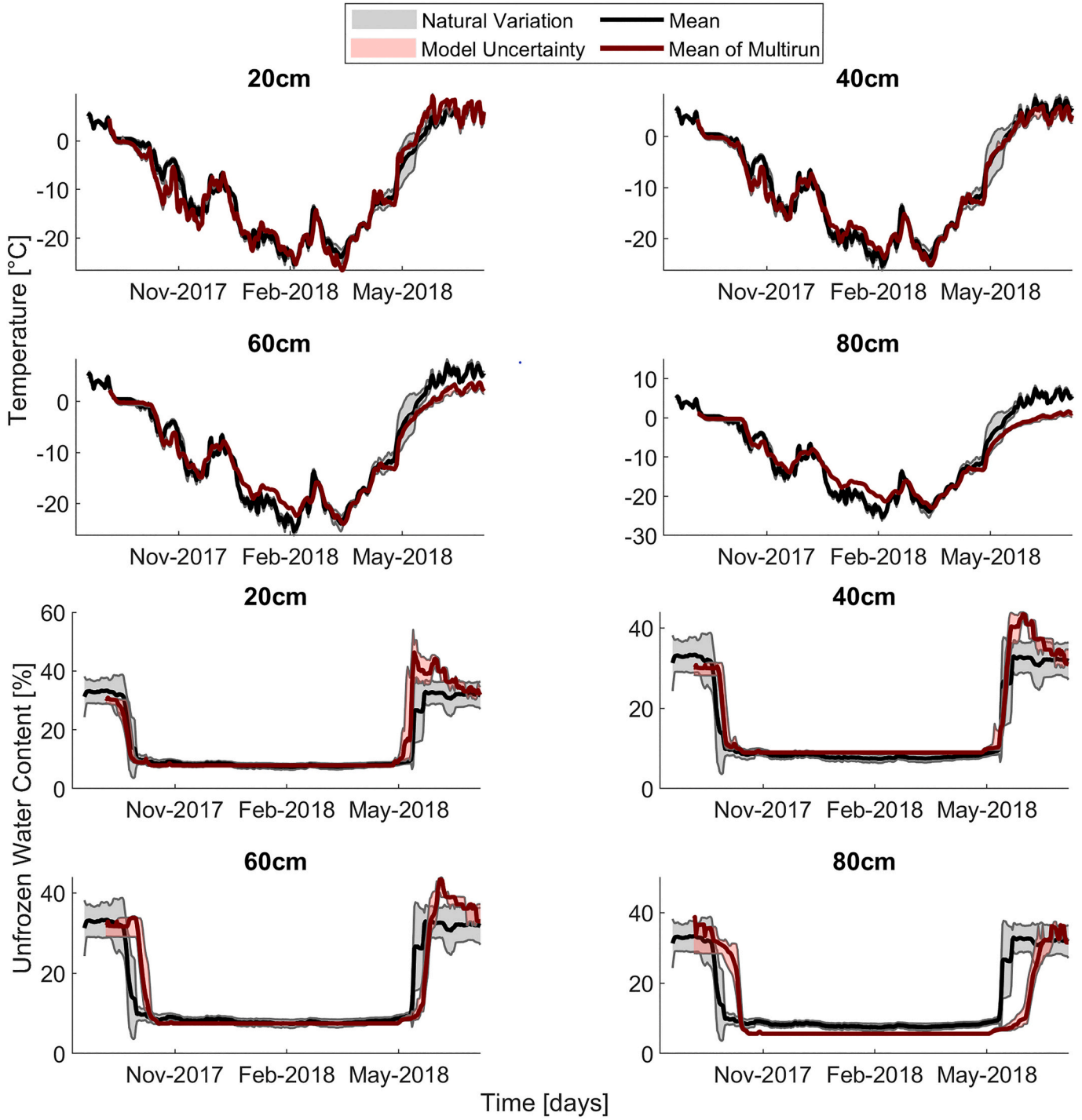

Fig. 8. Calibration results for temperature and water content at 20, 40, 60, 80 cm. Shown in the gray shaded area, are measurements from 6 field locations representing natural variation occurring on the slope. Shown in the red shaded area is the model uncertainty based on 10 best performing model runs, based on Monte Carlo GLUE calibration of 11 parameters. See Fig. S14 for validation results.

Accumulated drainage in the year one after the treatment was 33 mm lower for the H scenario than for the other scenarios, an effect of the relative lower water table at the beginning of the year in this scenario, thus removing water stored in the soil (Fig. S15). For the following year, accumulated surface runoff, drainage, and total runoff were comparable and within 5 mm of each other.

Although the accumulated values did not differ significantly, the daily drainage pattern between the scenarios differ in form of intensity and frequency (Fig. 10): The earlier thawing of the active layer to the depth of water saturated sediments in L allows for drainage above 2 mm to occur three days earlier than in C and ten days earlier than in H. The thicker saturated zone further allowed for higher daily drainage, with maximum flow in the L plot exceeding twice the max drainage in the H plot for the first year. For year two after the change, the difference between H and L became non-significant, but noted as the maximum drainage in the H plot was 2.1 mm less than at C and 1.7 mm higher at L (Table 7). This shift in frequency and intensity of drainage is expressed in the frequency distribution of drainage events. For all scenarios, small events (<0.5 mm/d) dominated the drainage with 362 for L, 149 in C and 196 in H. Intermediate drainage events (2–4 mm/d) occur 1.6 times

Table 5
Statistical Performance Values (NSE) for the model run. NSE is marked with asterisk: '*' very good, '**' good, '***' acceptable,'****' unsatisfactory (categories from Ritter and Muñoz-Carpena (2013)).

	Depth [cm]	Temperature	Water content
Calibration	20	0.93*	0.88**
	40	0.95*	0.92*
	60	0.96*	0.95*
	80	0.94*	0.93*
Validation	30	0.93*	0.71***
	60	0.95*	0.80**
	90	0.96*	0.78***
	120	0.94*	0.63****

more often in the H scenario than in the L case. But L showed fewer, more intense events with daily drainage exceeding 17.6 mm/day.

4. Discussion

4.1.1. Climate changes in Qaanaaq

The annual air temperature in Qaanaaq has increased 0.38 °C per decade from 1950 until 2020, which is aligned with observations for the entirety of Greenland, which has been reported to be 0.37 °C per decade for the period between 1961 and 2015 (Morice et al., 2021). The warming rate has increased from 0.33 °C per decade before 1990 to 0.48 °C per decade after 1990, where both values are on the lower end of the rate of change predicted by the CMIP5, RCP4.5 scenario (Smith et al., 2015), but reflect the acceleration of warming.

Analysis of seasonal data from the Qaanaaq and Thule area reveals that warmer winters are balanced by colder summers for the period 1990–2020. The importance of seasonal patterns in climate trends in Greenland was also observed by Westergaard-Nielsen et al. (2018), who highlighted that significant variations exist not only seasonally, but also regionally across Greenland.

Changes in the ratio of thawing and freezing degree days are important for assessing the risk of permafrost thawing. The ratio has increased significantly by a factor of 1.39 for the period 1990–2017 compared to a reference period from 1952 to 1990, which is likely to lead to a warmer and thicker active layer. This fits with analysis from Vikhamar-Schuler et al. (2016), who showed that 43% of the most extreme values of positive degree days occurred in the period 2000–2014 (total period 1894–2014) for eleven stations representing the Nordic arctic region.

The analysis stretching from 1950 until today roughly correlates with the time of permanent settlement in Qaanaaq, which began in 1953 (Hastrup, 2017), and the increase in thawing degree days points to that the active layer today exceeds thickness larger than in the last 70 years. This active layer thickening and the observed accelerated warming increases the risk that problems related to warming, which already exist today, are likely to become more severe in the future in Qaanaaq.

The effects of warming have already been observed in Qaanaaq in surface elevation changes of ice caps (Saito et al., 2016), leading to an

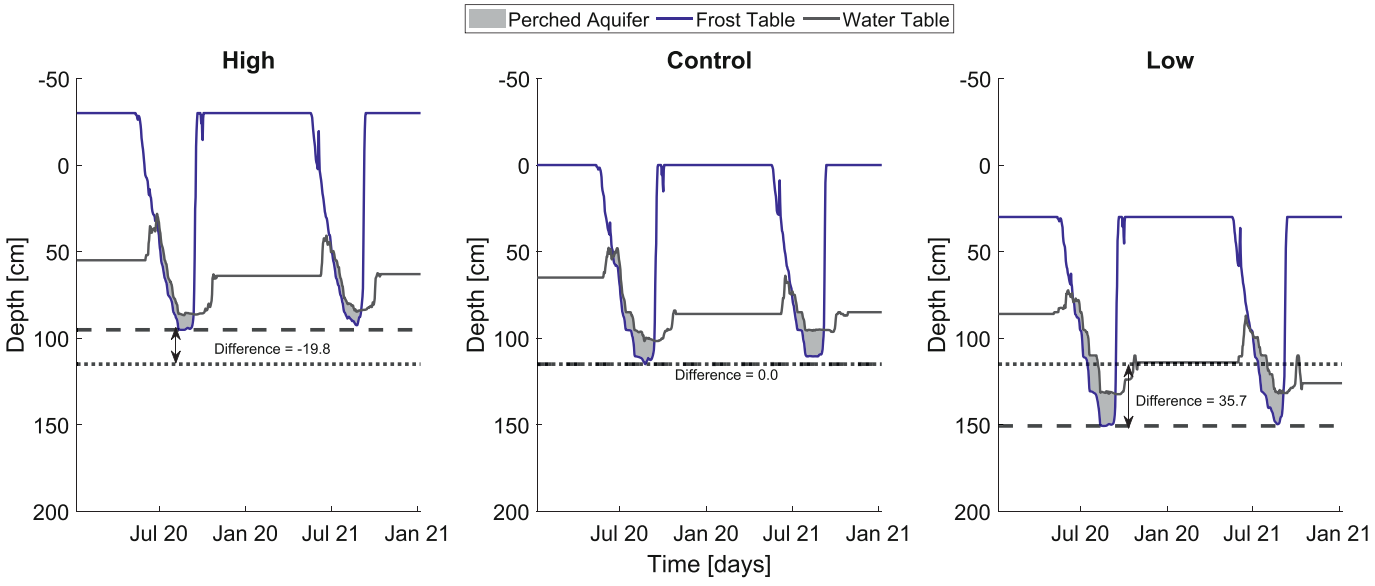

Fig. 9. Simulated depth to water (blue) and frost (black) level for the three scenarios in 2019 and 2020 and resulting difference in active layer thickness between the scenarios and changed thickness of the supra-permafrost aquifer (shaded area). Difference is relative to average active layer thickness from previous year.

Table 6
Dimensions of the perched supra permafrost aquifer in the model for the year 2019 / 2020.

Year	Duration				Max Thickness			
	Measurement	High	Control	Low	Measurement	High	Control	Low
2019	Depth Originating [cm]	32	53	79	Date	25.08	25.08	14.08
	Opening	24.06	17.06	14.06	Depth Water Table [cm]	85	100	131
	Closing	11.09	12.09	12.09	Depth Frost Table [cm]	95	115	151
	Duration [days]	79	85	89	Maximum Thickness [cm]	10	15	20
2020	Depth Originating [cm]	50	75	99	Date	23.08	04.08	27.08
	Opening	02.07	29.06	02.07	Depth Water Table [cm]	85	95	130
	Closing	03.09	07.09	04.09	Depth Frost Table [cm]	92	110	148
	Duration [days]	63	70	64	Maximum Thickness [cm]	7	15	18

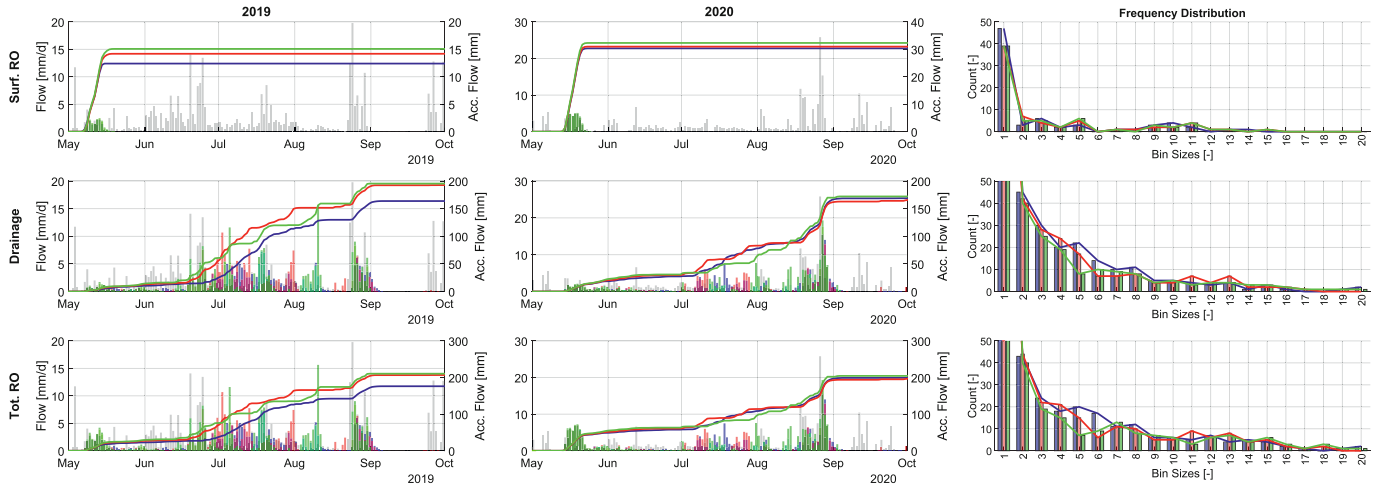

Fig. 10. Simulated drainage separated into surface runoff (top), drainage (middle) and total runoff (bottom) for the summer in year 2019 (left) and 2020 (center), for the high (blue), control (red) and low (green) scenario (Fig. S16 for graphs split by scenario). In shaded gray is measured precipitation. Right column shows the frequency distribution of daily drainage.

Table 7
Drainage from active layer in the years 2019/2020.

Year	Measurement	High	Control	Low
2019	Begin drainage	24.06	17.06	14.06
	max. daily drainage [mm/d]	7.3	10.1	15.6
	acc. total runoff [mm]	176	206	210
2020	Begin drainage	02.07	30.06	01.07
	max. daily drainage [mm/d]	15.5	17.6	19.3
	acc. total runoff [mm]	200	196	204

increase in glacial runoff and increasing the risk of flooding (Kondo et al., 2021). Observed beginning active layer detachment faults in the area around Qaanaaq show the beginning of accelerated erosion, which are expected with increasing air temperatures (Rowland et al., 2010). The slope on which the town and the experiment is located is not very steep, but the combination of the absence of continuous vegetation and a high content of coarse soil material is known to be vulnerable for erosion (Hao et al., 2021).

4.1.2. Active layer thickness and water table

The field experiment and the model scenarios in this study confirm that the change of the surface topography of 30 cm can create a marked response in the depth to permafrost. During the winter months, only protected depressions remain covered with snow for extended periods of time with more than a few cm of snow that is considered important as insulation for low air temperatures (Goncharova et al., 2019). The insulation and water storage from the snow in the actual experiment was about 30 cm and influenced the hydrothermal dynamics through the winter, and during the thawing phase in the beginning of summer. During the summer, the thickness of the saturated zone varied between the experimental plots according to the overall net positive water balance (precipitation>evaporation) and contrasting depth to permafrost (functioning as a hydraulic barrier). The difference in thickness of the saturated zone, and the associated changes in the bulk thermal properties of the soil (Farouki, 1981), leading to different propagation of thermal signals from the surface, thus temperatures at the base of the active layer that control the thaw/aggregation of permafrost.

The relation of snow and the active layer thickness has been well described by Atchley et al., 2016. This effect was also a major contributor to differences between observed and simulated responses of the treatment; in the field experiment during winter months and spring, the L plot was observed to be filled with snow. The insulation from that additional snow was evident as warmer temperatures during winter and reduced diurnal variations. The opposite was seen for the H plot with no snow cover at all. The combination of effects led to new permafrost being aggregated faster than existing permafrost thawing that in the field experiment.

In the model simulations, the variability of snow was not included in the models different scenarios, leading to the thermal conditions in the soil being the dominating effect. High thermal conductivity in the L scenario from a thick saturated layer, and a water table being located closer to the warming up of the surface allowed for rapid warming at the active layer base, thawing the permafrost. The thinner saturated layer in the H scenario and the larger distance between surface and water table slowed down the aggregation of permafrost.

The effect of reduced heat transfer buffer in the active layer has been described by Wang et al. (2018) on natural thaw slumps. They related similar effects to changes in water flow, but also to the depletion of organic carbon from destroyed plant material. This process is also likely to have occurred in the presented experiment. The relevance of water content and movement for the thawing of permafrost has also been shown in respect to fires (Zipper et al., 2018), where the reduction of groundwater recharge reduced the adjective heat transport in the active layer. The effects observed in the field experiment, including snow accumulation, as well as observations from model simulation, with the effect of changes in thermal properties of the soil have been described by Lafrenière and Lamoureux (2019), who further explain the importance of hydrological connectivity, which explains that the water table in active layer faults is kept stable due to sources from the catchment. This stabilization of the water table has both been observed in the field experiment and replicated in the model simulations.

4.1.3. Runoff and implications for the local hydrological regime

Lateral soil drainage only occurs when the soil is thawed, a hydraulic gradient exists, and a saturated layer is formed (Quinton et al., 2009). As shown, the perturbation of the surface alters the timing and depth of a thawed active layer and the thickness of a saturated layer, effectively controlling the transmissivity of the supra-permafrost aquifer and thus the flux that can potentially occur in the active layer. As a result, flows in response to precipitation events in the summer were larger in the L scenario compared to the C scenario or the H scenario. In the H scenario, flow is more gradually distributed over the year. The decrease of daily drainage in the H scenario, is larger than the increase in the L scenario, compared to the control, indicating that the control is already close to the maximum possible drainage the hydraulic gradient of 0.05 permits.

From the model scenarios, where influx from precipitation and temperature to the system were kept identical, several effects can be

observed: (1) The relatively lower water table at the beginning of the thawing period in the H scenario reduces the total runoff, as the low water content prohibits drainage, until infiltration into the soil raises the water content to saturation. (2) Ignoring the redistribution of snow, the active layer at L thaws earlier and leads to an earlier occurrence of drainage, with the inverse effect for H site. (3) Throughout the year, drainage remains lower at H site, than at the other scenarios, as the transmissivity is the limiting factor for the drainage. (4) After larger precipitation events, the overall higher transmissivity in the L scenario allows for higher daily drainage flow. (5) During the second year, simulations suggest that above-mentioned effects have disappeared, as the water table in the model has reached a new steady state.

To understand the ecosystem interactions with the water-soluble nutrients (such as nitrate), it is important to distinguish between surface flow and drainage, as the latter interacts with roots and microorganisms, moving nutrients and carbon within the soil (Rowland et al., 2010; Vonk and Gustafsson, 2013). Also the timing during the year (Lacroix et al., 2022), and movement velocity of nutrients (Pedersen et al., 2022), need to be considered when understanding the importance of water movement for the ecosystem. In the model scenarios, all components (runoff/drainage, timing, velocity) were influenced by the change of the surface, highlighting the importance of surface topography for the ecosystem. Thawing of the transition layer has occurred on the L plot in the field experiment and the model scenario. The faster flow in the L scenario can also have physical effects, when water is resurfacing at a later point, where flow of water can initiate and accelerate erosion (Fortier et al., 2007). For the town of Qaanaaq, this means that even small pits dug for construction can exacerbate the existing problems with surface water degrading roads and houses in the city.

4.1.4. Shortcomings and future research needs

The combination of a field experiment with a location specific physical model gained new insights in the quantification of soil drainage following erosion events. The role of snow in the propagation of temperature and its effect on the water movement in the soil was explored in one-dimension but with a lateral drainage (pseudo two-dimensional). The effects of the treatments on the active layer thickness were different in model and observations, but can be explained by the insulating effect of snow. The use of a snow distribution model (e.g. Li and Heap (2014)) may come as great aid in simulating the three-dimensional redistribution of snow.

The use of the one-dimensional model has the inherent shortcoming of neglecting three-dimensional effects. Although the relatively large size of the experiment plots diminished boundary effects on the center of the plots, differences in the flow regimes around the plots indicate that the hydrology in the vicinity was affected by the plots, by routing water flows towards the low plot and around the high plot. The choice of 10 m width was in accordance with the mean observed width of erosion gullies of 9.2 m (Dube et al., 2020), and the surface change of 30 cm is comparable to natural thaw slumps (Wang et al., 2018) and excavations made in the community. The experiment setup thus allows for comparison to natural erosion features of a similar size, as well as construction features in town. Larger erosion features, such as slope disturbances (Lamoureux et al., 2014), or the formation of thermokarst (Osterkamp et al., 2009) exhibit different processes such as tunneling (Fortier et al., 2007).

This work investigates effects from erosion and infrastructure under a current climate and does not take into account future changes in temperature and precipitation patterns. Using future climate scenarios like Copernicus Climate Change Service, C. D. S (2021) to investigate the development of surface changes is likely to produce new knowledge with relevance to the processes in periglacial environments and the local community in Qaanaaq.

5. Conclusion

The town Qaanaaq in NW Greenland is located on a hill and surface runoff. Therefore, flooding and water damage have often been seen in downslope areas even after minor construction work. Analysis of temperature observations from 1950 to 2020 reveal a warming trend of 0.38 °C per decade with the strongest warming in the 1990s and mainly in winter.

The field experiment and the model work show that physical topography changes of 30 cm can change the active layer depth and thereby the hydrological conditions. The discrepancy between changes in the frost table compared to the relatively smaller responses of the water table, result in different drainage patterns: From field and model results, we conclude that a minor lowering of the surface (30 cm), drainage occurs earlier in the year, and with higher intensity events. In contrast, raising the surface level leads to later and slower drainage. Also, the propagation of heat at the beginning of summer was shifted by several days, and model simulations showed drainage from the scenarios occurring with an offset of one week between the scenarios.

Both thickness of the supra permafrost aquifer and drainage behavior of the active layer are linked to other processes, such as snow cover, plant growth, water availability, nutrient transport and erosion. While the current study focuses on processes under the current climate, the effects observed are all expected to become more extreme under a warming climate and potentially affect larger areas of the landscape. This increased relevance and urgency calls for more research into the role of snow and the combined effort of physical and thermal perturbations.

The additional effect of snow is complex as it is determined by the timing of snowfall and redistribution with the wind. The results represented here, show that the response of permafrost to surface alteration may be different, depending on the snow cover. The resulting changes in the thaw depth and water flow mean that even minor construction in town can lead to water flow and flooding downhill and that meltwater management should be an integrated part in any construction work in town. A one-dimensional model, as used in this study may provide projections on the potential risk assessment of water flow, but our work also shows that a three-dimensional model including snow is recommended to provide a better understanding on water flow downhill a construction site.

Author statement

S.F.Z. and B.E. and T.I.N. designed the field experiment; S.F.Z. and T. I.N. conducted the fieldwork; S.F.Z. and W.Z. designed the model and performed the model runs. S.F.Z. analyzed the data and wrote the paper with contributions from all authors.

Declaration of Competing Interest

The authors declare that they have no known competing financial interests or personal relationships that could have appeared to influence the work reported in this paper.

Data availability

Data will be made available on request.

Acknowledgements

This work was supported by the Danish National Research Foundation (Center for Permafrost, CENPERM DNRF100). W. Z. was supported by the grants from Swedish Research Council VR (2020–05338) and Swedish National Space Agency (209/19). We thank ASIAQ, especially Kirsty Langley, for providing the climate data from the Airport Qaanaaq. We thank Per-Erik Jansson for the time to discuss the model set up and

suggest how to improve the model results. We appreciate the help of the students of the 2017 DTU ARTEK field group that assisted with collecting many samples. We are grateful to the many local people in Qaanaaq that were hospitable and helpful, especially to Kim Petersen who helped with accommodation and the installation of the field experiment and Dan D. Norman for allowing us to engage the local school in parts of the project. We appreciate the constructive feedback by two anonymous reviewers and editors on previous versions of the manuscript. This study is a contribution to the strategic research areas Modeling the Regional and Global Earth System (MERGE) and Biodiversity and Ecosystem Services in a Changing Climate (BECC) at Lund University.

Appendix A. Supplementary data

Supplementary data to this article can be found online at https://doi.org/10.1016/j.coldregions.2023.103899.

References

Atchley, A.L., Painter, S.L., Harp, D.R., Coon, E.T., Wilson, C.J., Liljedahl, A.K., Romanovsky, V.E., 2015. Using field observations to inform thermal hydrology models of permafrost dynamics with ATS (v0.83). Geosci. Model Dev. 8 (9), 2701–2722. https://doi.org/10.5194/gmd-8-2701-2015.

Atchley, A.L., Coon, E.T., Painter, S.L., Harp, D.R., Wilson, C.J., 2016. Influences and interactions of inundation, peat, and snow on active layer thickness. Geophys. Res. Lett. 43 (10), 5116–5123. https://doi.org/10.1002/2016gl068550.

Avannaata Kommunia, 2023. Fakta om kommunen. Retrieved 27.02.2023 from. https://www.avannaata.gl/emner/om_kommunen/fakta-om-kommunen?sc_lang=da.

Balland, V., Arp, P.A., 2005. Modeling soil thermal conductivities over a wide range of conditions. J. Environ. Eng. Sci. 4 (6), 549–558. https://doi.org/10.1139/s05-007.

Balser, A.W., Jones, J.B., Gens, R., 2014. Timing of retrogressive thaw slump initiation in the Noatak Basin, Northwest Alaska, USA. J. Geophys. Res. Earth Surf. 119 (5), 1106–1120.

Beel, C., Lamoureux, S., Orwin, J., 2018. Fluvial response to a period of hydrometeorological change and landscape disturbance in the Canadian High Arctic. Geophys. Res. Lett. 45 (19), 10,446-410,455.

Bintanja, R., Selten, F.M., 2014. Future increases in Arctic precipitation linked to local evaporation and sea-ice retreat. Nature 509 (7501), 479–482. https://doi.org/10.1038/nature13259.

Biskaborn, B.K., Smith, S.L., Noetzli, J., Matthes, H., Vieira, G., Streletskiy, D.A., Schoeneich, P., Romanovsky, V.E., Lewkowicz, A.G., Abramov, A., Allard, M., Boike, J., Cable, W.L., Christiansen, H.H., Delaloye, R., Diekmann, B., Drozdov, D., Etzelmuller, B., Grosse, G., Lantuit, H., 2019. Permafrost is warming at a global scale. Nat. Commun. 10 (1), 264. https://doi.org/10.1038/s41467-018-08240-4.

Blume, H.-P., Stahr, K., Leinweber, P., 2011. Bodenkundliches Praktikum: eine Einführung in pedologisches Arbeiten für Ökologen, insbesondere Land-und Forstwirte, und für Geowissenschaftler [Pedological practical training. An introduction in the pedological practice for ecologists, farmers, foresters and geoscientists], vol. 30. Springer.

Box, J.E., Colgan, W.T., Christensen, T.R., Schmidt, N.M., Lund, M., Parmentier, F.-J.W., Brown, R., Bhatt, U.S., Euskirchen, E.S., Romanovsky, V.E., Walsh, J.E., Overland, J. E., Wang, M., Corell, R.W., Meier, W.N., Wouters, B., Mernild, S., Mård, J., Pawlak, J., Olsen, M.S., 2019. Key indicators of Arctic climate change: 1971–2017. Environ. Res. Lett. 14 (4) https://doi.org/10.1088/1748-9326/aafc1b.

Brooks, R.H., Corey, A.T., 1966. Properties of porous media affecting fluid flow. J. Irrig. Drain. Div. 92 (2), 61–88.

Cappelen, J., Drost Jensen, C., 2021. In: Core Writing Team (Ed.), Climatological Standard Normals 1991-2020 – Greenland (2445-9127). Danish Meteorological Institute. https://www.dmi.dk/publikationer/.

Clarke, E.S., 2007. Permafrost foundation: state of the practice. Am. Soc. Civil Eng. https://doi.org/10.1061/9780784409473.

Connon, R., Devoie, É., Hayashi, M., Veness, T., Quinton, W., 2018. The Influence of Shallow Taliks on Permafrost Thaw and active Layer Dynamics in Subarctic Canada. J. Geophys. Res. Earth Surf. 123 (2), 281–297. https://doi.org/10.1002/2017jf004469.

Copernicus Climate Change Service, C. D. S, 2021. CMIP6 climate projections. Copernicus Climate Change Service (C3S) Climate Data Store (CDS) [Gridded]. https://doi.org/10.24381/cds.c866074c, 08-03-2023.

Dawes, P.R., 2006. Explanatory notes to the Geological map of Greenland, 1:500 000. Thule, Sheet 5. Geol. Surv. Den. Greenl. Map Ser. 2, 1–100. https://doi.org/10.34194/geusm.v2.4614.

Dobos, E., 2020. Albedo. In: Atmosphere and Climate. CRC Press, pp. 25–28.

Dube, H.B., Mutema, M., Muchaonyerwa, P., Poesen, J., Chaplot, V., 2020. A global analysis of the morphology of linear erosion features. Catena 190. https://doi.org/10.1016/j.catena.2020.104542.

Dye, H.B., Houston, S.L., Welfert, B.D., 2009. Influence of Unsaturated Soil Properties uncertainty on Moisture Flow Modeling. Geotech. Geol. Eng. 29 (2), 161–169. https://doi.org/10.1007/s10706-009-9281-0.

Evans, S.G., Ge, S., 2017. Contrasting hydrogeologic responses to warming in permafrost and seasonally frozen ground hillslopes. Geophys. Res. Lett. https://doi.org/10.1002/2016gl072009.

Farouki, O.T., 1981. The thermal properties of soils in cold regions. Cold Reg. Sci. Technol. 5 (1), 67–75. https://doi.org/10.1016/0165-232X(81)90041-0.

Fortier, D., Allard, M., Shur, Y., 2007. Observation of rapid drainage system development by thermal erosion of ice wedges on Bylot Island, Canadian Arctic Archipelago. Permafr. Periglac. Process. 18 (3), 229–243. https://doi.org/10.1002/ppp.595.

Frampton, A., Painter, S.L., Destouni, G., 2012. Permafrost degradation and subsurface-flow changes caused by surface warming trends. Hydrogeol. J. 21 (1), 271–280. https://doi.org/10.1007/s10040-012-0938-z.

Garzanti, E., 2019. Petrographic classification of sand and sandstone. Earth Sci. Rev. 192, 545–563. https://doi.org/10.1016/j.earscirev.2018.12.014.

GEUS, 2012. Seamless Digital 1:500 000 Scale Geological Map of Greenland. Geological Survey of Denmark and Greenland (GEUS). https://data.geus.dk/MetaVis/XMLService.jsp?id=2378.

Goncharova, O.Y., Matyshak, G.V., Epstein, H.E., Sefilian, A.R., Bobrik, A.A., 2019. Influence of snow cover on soil temperatures: Meso- and micro-scale topographic effects (a case study from the northern West Siberia discontinuous permafrost zone). Catena 183. https://doi.org/10.1016/j.catena.2019.104224.

Goudriaan, J., Van Laar, H., 2012. Modelling Potential Crop Growth Processes: Textbook with Exercises, vol. 2. Springer Science & Business Media.

Hansen, B.U., Elberling, B., Humlum, O., Nielsen, N., 2006. Meteorological trends (1991–2004) at Arctic Station, Central West Greenland (69°15'N) in a 130 years perspective. Geogr. Tidsskr. Dan. J. Geogr. 106 (1), 45–55. https://doi.org/10.1080/00167223.2006.10649544.

Hao, H.-X., Qin, J.-H., Sun, Z.-X., Guo, Z.-L., Wang, J.-G., 2021. Erosion-reducing effects of plant roots during concentrated flow under contrasting textured soils. Catena 203, 105378. https://doi.org/10.1016/j.catena.2021.105378.

Hastrup, K., 2017. The Viability of a High Arctic Hunting Community: A Historical Perspective. In: Brightman, M., Lewis, J. (Eds.), The Anthropology of Sustainability: Beyond Development and Progress. Palgrave Macmillan US, pp. 145–163. https://doi.org/10.1057/978-1-137-56636-2_9.

Hendriksen, K., Hoffmann, B., 2016. Qaanaaq Distrikt – infrastruktur og erhvervsgrundlag: Sammenfatning af pilotprojekt om lokal baseret erhvervsudvikling. Qaanaaq District – infrastructure and income basis: Summary of a pilot project on local based business development. Center for Arktisk Teknologi.

Henriksen, N., Higgins, A., Kalsbeek, F., Pulvertaft, T.C.R., 2009. Greenland from Archaean to Quaternary. Descriptive text to the 1995 Geological map of Greenland, 1: 2 500 000. GEUS Bull. 18, 1–126. https://doi.org/10.34194/geusb.v18.4993.

Hjort, J., Karjalainen, O., Aalto, J., Westermann, S., Romanovsky, V.E., Nelson, F.E., Etzelmuller, B., Luoto, M., 2018. Degrading permafrost puts Arctic infrastructure at risk by mid-century. Nat. Commun. 9 (1), 5147. https://doi.org/10.1038/s41467-018-07557-4.

Hjort, J., Streletskiy, D., Doré, G., Wu, Q., Bjella, K., Luoto, M., 2022. Impacts of permafrost degradation on infrastructure. Nat. Rev. Earth Environ. 3 (1), 24–38. https://doi.org/10.1038/s43017-021-00247-8.

Hollesen, J., Elberling, B., Jansson, P.E., 2011. Future active layer dynamics and carbon dioxide production from thawing permafrost layers in Northeast Greenland. Glob. Chang. Biol. 17 (2), 911–926. https://doi.org/10.1111/j.1365-2486.2010.02256.x.

Ingeman-Nielsen, T., Lemay, M., Allard, M., Barrette, C., Bjella, K., Brooks, H., Carbonneau, A.-S., Doré, G., Foged, N., Lading, T., 2018. Built infrastructure. In: Adaptation Actions for a Changing Arctic: Perspectives from the Baffin Bay/Davis Strait Region. Arctic Monitoring and Assessment Programme (AMAP), pp. 261–306.

Ingeman-Nielsen, T., Tomaskovicova, S., Foged, N., 2020. Ground Temperatures Qaanaaq. Technical University of Denmark, Department of Civil Engineering.

IPCC, 2021. In: Masson-Delmotte, V., Zhai, P., Pirani, A., Connors, S.L., Péan, C., Berger, S., Caud, N., Chen, Y., Goldfarb, L., Gomis, M. (Eds.), Climate Change 2021: The Physical Science Basis, vol. 2. Cambridge University Press. https://doi.org/10.1017/9781009157896.

Jansson, P.-E., 2004. Coupled Heat and Mass Transfer Model for Soil-Plant-Atmosphere Systems. ftp://www.lwr.kth.se/CoupModel/CoupModel.pdf. https://cir.nii.ac.jp/crid/1571135650917386112.

Jansson, P.-E., 2012. CoupModel: model use, calibration, and validation. Trans. ASABE 55 (4), 1337–1344. https://doi.org/10.13031/2013.42245.

Jorgenson, M.T., Romanovsky, V., Harden, J., Shur, Y., O'Donnell, J., Schuur, E.A., Kanevskiy, M., Marchenko, S., 2010. Resilience and vulnerability of permafrost to climate change. Can. J. For. Res. 40 (7), 1219–1236.

Kalnay, E., Kanamitsu, M., Kistler, R., Collins, W., Deaven, D., Gandin, L., Iredell, M., Saha, S., White, G., Woollen, J., 1996. The NCEP/NCAR 40-year reanalysis project. Bull. Am. Meteorol. Soc. 77 (3), 437–472.

Karjalainen, O., Luoto, M., Aalto, J., Etzelmüller, B., Grosse, G., Jones, B.M., Lilleøren, K. S., Hjort, J., 2020. High potential for loss of permafrost landforms in a changing climate. Environ. Res. Lett. 15 (10) https://doi.org/10.1088/1748-9326/abafd5.

Kondo, K., Sugiyama, S., Sakakibara, D., Fukumoto, S., 2021. Flood events caused by discharge from Qaanaaq Glacier, northwestern Greenland. J. Glaciol. 67 (263), 500–510. https://doi.org/10.1017/jog.2021.3.

Kottek, M., Grieser, J., Beck, C., Rudolf, B., Rubel, F., 2006. World Map of the Köppen-Geiger Climate Classification Updated. https://doi.org/10.1127/0941-2948/2006/0130.

Kurylyk, B.L., Watanabe, K., 2013. The mathematical representation of freezing and thawing processes in variably-saturated, non-deformable soils. Adv. Water Resour. 60, 160–177. https://doi.org/10.1016/j.advwatres.2013.07.016.

Kurylyk, B.L., MacQuarrie, K.T.B., McKenzie, J.M., 2014a. Climate change impacts on groundwater and soil temperatures in cold and temperate regions: Implications,

mathematical theory, and emerging simulation tools. Earth Sci. Rev. 138, 313–334. https://doi.org/10.1016/j.earscirev.2014.06.006.
Kurylyk, B.L., McKenzie, J.M., MacQuarrie, K.T.B., Voss, C.I., 2014b. Analytical solutions for benchmarking cold regions subsurface water flow and energy transport models: One-dimensional soil thaw with conduction and advection. Adv. Water Resour. 70, 172–184. https://doi.org/10.1016/j.advwatres.2014.05.005.
Lacroix, F., Zaehle, S., Caldararu, S., Schaller, J., Stimmler, P., Holl, D., Kutzbach, L., Gockede, M., 2022. Mismatch of N release from the permafrost and vegetative uptake opens pathways of increasing nitrous oxide emissions in the high Arctic. Glob. Chang. Biol. 28 (20), 5973–5990. https://doi.org/10.1111/gcb.16345.
Lafrenière, M.J., Lamoureux, S.F., 2019. Effects of changing permafrost conditions on hydrological processes and fluvial fluxes. Earth Sci. Rev. 191, 212–223. https://doi.org/10.1016/j.earscirev.2019.02.018.
Lal, R., 2019. Accelerated Soil erosion as a source of atmospheric CO2. Soil Tillage Res. 188, 35–40. https://doi.org/10.1016/j.still.2018.02.001.
Lamhonwah, D., Lafrenière, M.J., Lamoureux, S.F., Wolfe, B.B., 2017. Evaluating the hydrological and hydrochemical responses of a High Arctic catchment during an exceptionally warm summer. Hydrol. Process. 31 (12), 2296–2313. https://doi.org/10.1002/hyp.11191.
Lamontagne-Hallé, P., McKenzie, J.M., Kurylyk, B.L., Zipper, S.C., 2018. Changing groundwater discharge dynamics in permafrost regions. Environ. Res. Lett. 13 (8) https://doi.org/10.1088/1748-9326/aad404.
Lamoureux, S.F., Lafrenière, M.J., Favaro, E.A., 2014. Erosion dynamics following localized permafrost slope disturbances. Geophys. Res. Lett. 41 (15), 5499–5505.
Lantz, T.C., Kokelj, S.V., Gergel, S.E., Henry, G.H., 2009. Relative impacts of disturbance and temperature: persistent changes in microenvironment and vegetation in retrogressive thaw slumps. Glob. Chang. Biol. 15 (7), 1664–1675.
Lewkowicz, A.G., 2007. Dynamics of active-layer detachment failures, Fosheim peninsula, Ellesmere Island, Nunavut, Canada. Permafr. Periglac. Process. 18 (1), 89–103.
Li, J., Heap, A.D., 2014. Spatial interpolation methods applied in the environmental sciences: a review. Environ. Model. Softw. 53, 173–189. https://doi.org/10.1016/j.envsoft.2013.12.008.
Li, L., Pomeroy, J.W., 1997. Probability of occurrence of blowing snow. J. Geophys. Res.-Atmos. 102 (D18), 21955–21964.
Liljedahl, A.K., Boike, J., Daanen, R.P., Fedorov, A.N., Frost, G.V., Grosse, G., Hinzman, L.D., Iijma, Y., Jorgenson, J.C., Matveyeva, N., Necsoiu, M., Raynolds, M. K., Romanovsky, V.E., Schulla, J., Tape, K.D., Walker, D.A., Wilson, C.J., Yabuki, H., Zona, D., 2016. Pan-Arctic ice-wedge degradation in warming permafrost and its influence on tundra hydrology. Nat. Geosci. 9 (4), 312–318. https://doi.org/10.1038/ngeo2674.
Matzner, E., Borken, W., 2008. Do freeze-thaw events enhance C and N losses from soils of different ecosystems? A review. Eur. J. Soil Sci. 59 (2), 274–284. https://doi.org/10.1111/j.1365-2389.2007.00992.x.
Menne, M.J., Durre, I., Korzeniewski, B., McNeal, S., Thomas, K., Yin, X., Anthony, S., Ray, R., Vose, R., Gleason, B., 2012. Global Historical Climatology Network-Daily (Version 3.24). GHCND:GLW00017605. https://doi.org/10.7289/V5D21VHZ 2020-03-03.
Morice, C.P., Kennedy, J.J., Rayner, N.A., Winn, J.P., Hogan, E., Killick, R.E., Dunn, R.J. H., Osborn, T.J., Jones, P.D., Simpson, I.R., 2021. An Updated Assessment of Near-Surface Temperature Change from 1850: the HadCRUT5 Data Set. J. Geophys. Res.-Atmos. 126 (3) https://doi.org/10.1029/2019jd032361.
Nash, J.E., Sutcliffe, J.V., 1970. River flow forecasting through conceptual models part I—A discussion of principles. J. Hydrol. 10 (3), 282–290.
Obu, J., Westermann, S., Bartsch, A., Berdnikov, N., Christiansen, H.H., Dashtseren, A., Delaloye, R., Elberling, B., Etzelmüller, B., Kholodov, A., Khomutov, A., Kääb, A., Leibman, M.O., Lewkowicz, A.G., Panda, S.K., Romanovsky, V., Way, R.G., Westergaard-Nielsen, A., Wu, T., Zou, D., 2019. Northern Hemisphere permafrost map based on TTOP modelling for 2000–2016 at 1 km2 scale. Earth Sci. Rev. 193, 299–316. https://doi.org/10.1016/j.earscirev.2019.04.023.
O'Connor, M.T., Cardenas, M.B., Neilson, B.T., Nicholaides, K.D., Kling, G.W., 2019. Active Layer Groundwater Flow: the Interrelated Effects of Stratigraphy, Thaw, and Topography. Water Resour. Res. 55 (8), 6555–6576. https://doi.org/10.1029/2018wr024636.
Okkonen, J., Ala-Aho, P., Hänninen, P., Hayashi, M., Sutinen, R., Liwata, P., 2017. Multi-year simulation and model calibration of soil moisture and temperature profiles in till soil. Eur. J. Soil Sci. 68 (6), 829–839. https://doi.org/10.1111/ejss.12489.
Osterkamp, T., Jorgenson, M., Schuur, E., Shur, Y., Kanevskiy, M., Vogel, J., Tumskoy, V., 2009. Physical and ecological changes associated with warming permafrost and thermokarst in interior Alaska. Permafr. Periglac. Process. 20 (3), 235–256.
Pedersen, E.P., Elberling, B., Michelsen, A., 2022. Upslope release—Downslope receipt? Multi-year plant uptake of permafrost-released nitrogen along an arctic hillslope. J. Ecol. 110 (8), 1896–1912. https://doi.org/10.1111/1365-2745.13925.
Pribyl, D.W., 2010. A critical review of the conventional SOC to SOM conversion factor. Geoderma 156 (3–4), 75–83. https://doi.org/10.1016/j.geoderma.2010.02.003.
Quinton, W.L., Bemrose, R.K., Zhang, Y., Carey, S.K., 2009. The influence of spatial variability in snowmelt and active layer thaw on hillslope drainage for an alpine tundra hillslope. Hydrol. Process.: Int. J. 23 (18), 2628–2639.
Rasmussen, L.H., Zhang, W., Hollesen, J., Cable, S., Christiansen, H.H., Jansson, P.-E., Elberling, B., 2018. Modelling present and future permafrost thermal regimes in Northeast Greenland. Cold Reg. Sci. Technol. 146, 199–213. https://doi.org/10.1016/j.coldregions.2017.10.011.
Rawls, W.J., Brakensiek, D.L., Saxtonn, K., 1982. Estimation of soil water properties. Trans. ASAE 25 (5), 1316–1320.
Richards, L.A., 1931. Capillary conduction of liquids through porous mediums. Physics 1 (5), 318–333.
Ritter, A., Muñoz-Carpena, R., 2013. Performance evaluation of hydrological models: Statistical significance for reducing subjectivity in goodness-of-fit assessments. J. Hydrol. 480, 33–45. https://doi.org/10.1016/j.jhydrol.2012.12.004.
Rowland, J.C., Jones, C.E., Altmann, G., Bryan, R., Crosby, B.T., Hinzman, L.D., Kane, D. L., Lawrence, D.M., Mancino, A., Marsh, P., McNamara, J.P., Romanvosky, V.E., Toniolo, H., Travis, B.J., Trochim, E., Wilson, C.J., Geernaert, G.L., 2010. Arctic Landscapes in transition: responses to Thawing Permafrost. EOS Trans. Am. Geophys. Union 91 (26), 229–230. https://doi.org/10.1029/2010EO260001.
Saito, J., Sugiyama, S., Tsutaki, S., Sawagaki, T., 2016. Surface elevation change on ice caps in the Qaanaaq region, northwestern Greenland. Polar Sci. 10 (3), 239–248. https://doi.org/10.1016/j.polar.2016.05.002.
Schädel, C., 2022. Arctic coasts predicted to erode. Nat. Clim. Chang. 12 (3), 224–225. https://doi.org/10.1038/s41558-022-01286-9.
Schuh, C., Frampton, A., Christiansen, H.H., 2017. Soil moisture redistribution and its effect on inter-annual active layer temperature and thickness variations in a dry loess terrace in Adventdalen, Svalbard. Cryosphere 11 (1), 635–651.
Sjöberg, Y., Jan, A., Painter, S.L., Coon, E.T., Carey, M.P., O'Donnell, J.A., Koch, J.C., 2021. Permafrost Promotes Shallow Groundwater Flow and Warmer Headwater Streams. Water Resour. Res. 57 (2) https://doi.org/10.1029/2020wr027463.
Smith, S.J., Edmonds, J., Hartin, C.A., Mundra, A., Calvin, K., 2015. Near-term acceleration in the rate of temperature change. Nat. Clim. Chang. 5 (4), 333–336.
Strand, S.M., Christiansen, H.H., Johansson, M., Åkerman, J., Humlum, O., 2020. Active layer thickening and controls on interannual variability in the Nordic Arctic compared to the circum-Arctic. Permafr. Periglac. Process. 32 (1), 47–58. https://doi.org/10.1002/ppp.2088.
Subcommittee, Permafrost, 1988. In: Core Writing Team, H. S.A., F. H.M., H. J.A., J. G. H., L. B., S. D.C., & v. E. R.O (Ed.), Glossary of Permafrost and Related Ground-Ice Terms. National Research Council of Canada, Ottawa, Ontario, Canada. Associate Committee on Geotechnical Research, National Research Council of Canada, Ottawa.
Vaughn, D.M., 2005. Degree Days. In: Oliver, J.E. (Ed.), Encyclopedia of World Climatology. Springer, Netherlands, pp. 315–318. https://doi.org/10.1007/1-4020-3266-8_64.
Vikhamar-Schuler, D., Isaksen, K., Haugen, J.E., Tømmervik, H., Luks, B., Schuler, T.V., Bjerke, J.W., 2016. Changes in winter warming events in the Nordic Arctic Region. J. Clim. 29 (17), 6223–6244. https://doi.org/10.1175/JCLI-D-15-0763.1.
Vincent, W.F., Callaghan, T.V., Dahl-Jensen, D., Johansson, M., Kovacs, K.M., Michel, C., Prowse, T., Reist, J.D., Sharp, M., 2012. Ecological implications of changes in the arctic cryosphere. Ambio 40 (S1), 87–99. https://doi.org/10.1007/s13280-011-0218-5.
von Storch, H., Zwiers, F.W., 1999. Regression. In: Statistical Analysis in Climate Research. Cambridge University Press, pp. 145–170. https://doi.org/10.1017/CBO9780511612336.009.
Vonk, J.E., Gustafsson, Ö., 2013. Permafrost-carbon complexities. Nat. Geosci. 6 (9), 675–676.
Walvoord, M.A., Kurylyk, B.L., 2016. Hydrologic Impacts of Thawing Permafrost-a Review. Vadose Zone J. 15 (6) https://doi.org/10.2136/vzj2016.01.0010.
Wang, Y., Sun, Z., Sun, Y., 2018. Effects of a thaw slump on active layer in permafrost regions with the comparison of effects of thermokarst lakes on the Qinghai–Tibet Plateau, China. Geoderma 314, 47–57. https://doi.org/10.1016/j.geoderma.2017.10.046.
Westergaard-Nielsen, A., Karami, M., Hansen, B.U., Westermann, S., Elberling, B., 2018. Contrasting temperature trends across the ice-free part of Greenland. Sci. Rep. 8 (1), 1586. https://doi.org/10.1038/s41598-018-19992-w.
Woo, M.-K., 2012. Permafrost Hydrology. Springer Science & Business Media. https://doi.org/10.1007/978-3-642-23462-0.
Wu, S.H., Jansson, P.E., Zhang, X.Y., 2011. Modelling temperature, moisture and surface heat balance in bare soil under seasonal frost conditions in China. Eur. J. Soil Sci. 62 (6), 780–796. https://doi.org/10.1111/j.1365-2389.2011.01397.x.
Young, K.L., Assini, J., Abnizova, A., Miller, E.A., 2013. Snowcover and melt characteristics of upland/lowland terrain: Polar Bear Pass, Bathurst Island, Nunavut, Canada. Hydrol. Res. 44 (1), 2–20.
Zhang, W., Jansson, P.-E., Schurgers, G., Hollesen, J., Lund, M., Abermann, J., Elberling, B., 2018. Process-Oriented Modeling of a High Arctic Tundra Ecosystem: Long-Term Carbon Budget and Ecosystem responses to Interannual Variations of climate. J. Geophys. Res. Biogeosci. 123 (4), 1178–1196. https://doi.org/10.1002/2017jg003956.
Zhang, W., Jansson, P.-E., Sigsgaard, C., McConnell, A., Jammet, M.M., Westergaard-Nielsen, A., Lund, M., Friborg, T., Michelsen, A., Elberling, B., 2019. Model-data fusion to assess year-round CO2 fluxes for an arctic heath ecosystem in West Greenland (69°N). Agric. For. Meteorol. 272-273, 176–186. https://doi.org/10.1016/j.agrformet.2019.02.021.
Zipper, S.C., Lamontagne-Hallé, P., McKenzie, J.M., Rocha, A.V., 2018. Groundwater Controls on Postfire Permafrost Thaw: Water and Energy Balance Effects. J. Geophys. Res. Earth Surf. 123 (10), 2677–2694. https://doi.org/10.1029/2018jf004611.